UNIVERSITÀ DI PISA

Scuola di dottorato in Ingegneria "Leonardo da Vinci"

Corso di Dottorato di Ricerca in
TELERILEVAMENTO

Tesi di Dottorato di Ricerca

"Feasibility study and development of a full digital passive radar demonstrator"

Autore
Michele Conti

_____

Relatori
Prof. Marco Martorella

_____

Dr. Ing. Amerigo Capria

_____

SSD ING-INF/03

ABSTRACT

In the past few years we have witnessed a growing interest in Passive Radars which exploit electromagnetic emissions coming from non-cooperative transmitters for example TV/Radio stations. The main feature of these systems is the absence of a transmitter. This feature, in addition to reduced system costs, makes this kind of equipment hard to intercept.

Many demonstrators have been developed in the past decade by Universities, research facilities and private companies, however, we can't say we have found a solution to fully satisfy the performance and cost requirements.

This thesis focuses on the development of a low cost passive radar demonstrator with the aim of achieving a high range resolution exploiting the DVB-T signal as illuminator of opportunity (IO), which should satisfy both cost and performance needs.

The study and design of the above mentioned radar demonstrator lead to three main innovative aspects.

The first aspect is the realisation of a low cost passive radar demonstrator based on Software Defined Radio (SDR) technologies. In particular the Universal Software Radio Peripherals (USRPs) seems to be a good solution which meets the requirements of scalability and modularity which our system must have, for example the possibility to receive different signals by using the same hardware configured via software.

The second aspect is the development of the whole processing chain. A theoretical analysis and experimental validation for every algorithm have been done. In particular, all algorithms developed are independent from the type of illuminator of opportunity chosen. This advantage, in conjunction with the use of a hardware which can be reconfigured via software, makes the entire radar system adaptive to the signal used.

The third and final point focuses on the way to obtain a passive radar system which offers high range resolution. Specifically, in this thesis, the possibility of obtaining a high range resolution using adjacent DVB-T channels has been studied.

A theoretical analysis, followed by a validation on real data will highlight that the resolution enhancement is proportional to the number of exploited DVB-T channels.

The radar's functionality is tested on different scenarios: maritime and aerial. The experimental results obtained with the demonstrator in both scenarios for different types of targets is proved both the feasibility of our radar system and the actual improvement of range resolution resulting from using multiple DVB-T adjacent channels

ACRONYMS

ACF	Autocorrelation Function
ADC	Analog to Digital Converter
ADS-B	Automatic Dependent Surveillance - Broadcast
AF	Ambiguity Function
API	Application Programming Interface
CAF	Cross Ambiguity Function
CCF	Cross-Correlation Function
CNR	Clutter to Noise Ratio
COFDM	Coded Orthogonal Frequency-Division Multiplexing
COTS	Commercial Off-the-Shelf component
DAB	Digital Audio Broadcasting
DBPSK	Differential Binary Phase Shift Keying
DDC	Digital Down-Converter
DNR	Direct to Noise Ratio
DVB-T	Digital Video Broadcasting - Terrestrial
EIRP	Equivalent Isotropic Radiated Power
FFT	Fast Fourier Transform
FM	Frequency Modulation
GI	Guard Interval
GNU	Gnu is Not Unix
GSM	Global System for Mobile Communications
IO	Illuminator of Opportunity
LAN	Local Area Network
LIT	Long Integration Times
LNA	Low Noise Amplifier
LS	Least Squares
MIMO	Multiple-Input and Multiple-Output
MMSE	Minimum Mean Square Error
NLMS	Normalized Least Mean Squares

OFDM	Orthogonal Frequency-Division Multiplexing
PBR	Passive Bistatic Radar
PCI	Peripheral Component Interconnect
PCL	Passive Coherent Location
PCR	Passive Covert Radar
PRBS	Pseudorandom Binary Sequence
RAID	Redundant Array of Inexpensive Disks
RDA	Range-Doppler-Azimuth
RF	Radio Frequency
SDR	Software Defined Radio
SFN	Single Frequency Network
SINR	Signal Interference plus Noise Ratio
TPS	Transmission Parameters Signalling
UHD	Universal Hardware Driver
UHF	Ultra High Frequency
UMTS	Universal Mobile Telecommunications System
USB	Universal Serial Bus
USRP	Universal Software Radio Peripheral
VHF	Very High Frequency
Wi-Fi	Wireless Fidelity
WiMAX	Worldwide Interoperability for Microwave Access
ZF	Zero-Forcing

LIST OF FIGURES

LIST OF TABLES

CONTENTS

INTRODUCTION

Passive Bistatic Radar (PBR, also referred to as Passive Coherent Location) exploits Illuminators of Opportunity (IO) such as FM radio, DAB, analogue and digital television signals, GSM/UMTS base stations in order to detect and track targets. This system concept is of great interest in both civilian and military scenarios mainly due to number of advantages offered by this system with respect to active radar. A PBR system may benefit from an enhanced target Radar Cross Section (RCS) with respect to the monostatic case, thanks to the lower frequency of operation (i.e.: VHF and UHF bands) and the bistatic configuration. Moreover, it does not require any dedicated frequency band allocation, it allows covert surveillance and it can be developed with a reduced budget using low cost components thanks to the absence of the transmitter unit. This radar technology may also be realized by means of Software Defined Radio systems, which typically meet low cost requirements and guarantee system flexibility. The performance of a passive radar system strongly depends on the transmitted power and on the characteristics of the exploited IO, which is used as a reference signal. As the range coverage increases when the transmitted power level increases, high-power transmitters, such as broadcast FM, DAB radio, analogue and DVB television transmitters, are preferable.

Furthermore, in many countries, analogue radio and TV transmissions will be soon dismissed and will be replaced by digital ones. In summary, DVB-T transmitters should be considered to be one of the best candidates for passive radar purposes thanks to the high level of radiated power and to the good waveform performances in terms of range and Doppler resolution.

An ongoing research field about passive radar systems concerns the theoretical range resolution improvement achieved by using multiple FM channels and DVB-T channels. In this thesis, the possibility to improve the range resolution by using multiple adjacent DVB-T channels from the same transmitter will be addressed.

In this thesis a DVB-T Software Defined Passive Radar demonstrator will be developed, the whole processing chain will be described and tested. The hardware of the demonstrator will be presented.

Then the range resolution improvement will be obtained by considering multiple adjacent DVB-T channels as a single wideband signal. Furthermore experimental results obtained with our demonstrator in two different scenarios will be shown. The effective improvement on the range resolution will be underlined by comparing the results obtained for a single and multiple DVB-T channel operation.

.

Chapter 1.

PASSIVE BISTATIC RADAR SYSTEMS

1.1. PRINCIPLE

Passive Bistatic Radar (PBR) systems, also referred to as Passive Coherent Location (PCL) systems, exploit reflection from illuminators of opportunity (IO) in order to detect and track objects. A PBR receiver, as shown in Figure 1.1 , generally presents two receiving channels [1] denoted as reference channel and surveillance channel. The reference channel is used to capture the direct signal from the transmitter and provides a reference signal to be compared with the target return.

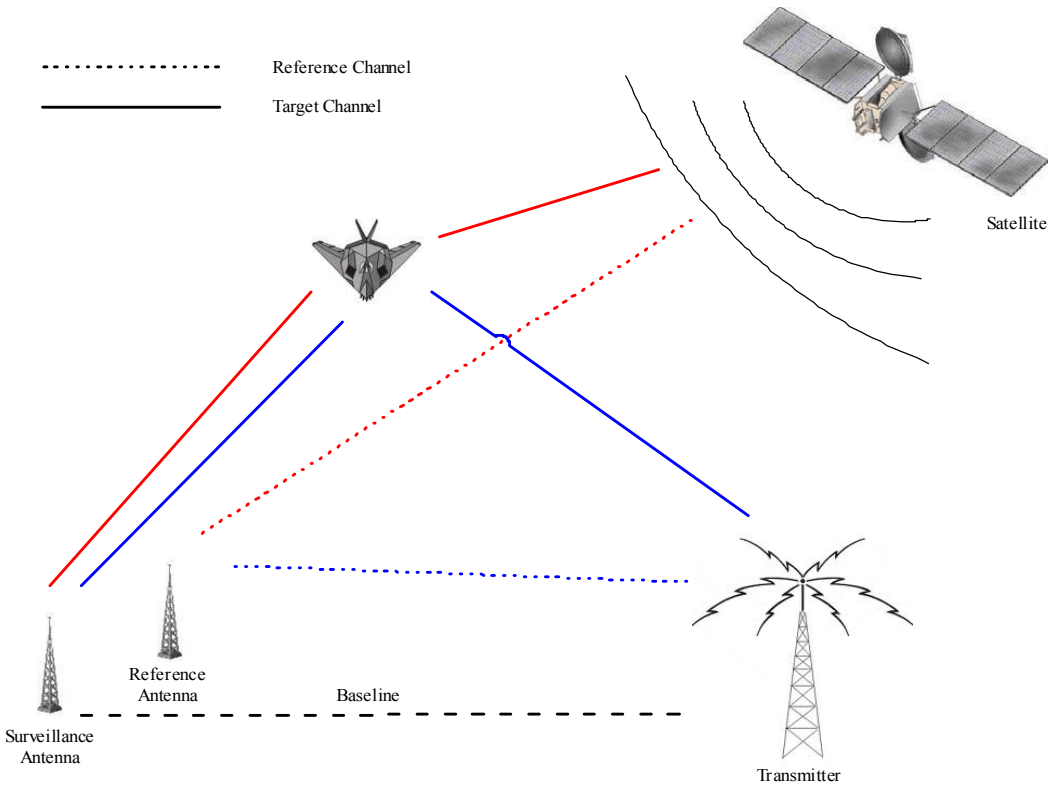

Figure 1.1 Passive Radar Concept

The comparison is usually carried out by a cross-correlation [2] between reference signal and the target signal and it actually represents the basic process to detect targets with a passive radar.

The application area of passive radars is strictly dependent on the illuminator of opportunity properties [3]. The important features of an illuminator of opportunity are: the power density values at the target, the coverage, the signal characteristics and its ambiguity properties.

The illuminators of opportunity can be divided into two main classes: analogue emitters like FM radio [4]-[6], analogue TV, or digital transmitter as DAB/DVB-T [7],[8], GSM [9], UTMS [10], Wi-Fi, WiMAX [11]. Passive radars based on analogue signals show detection performance strongly dependent on the signal content. In contrast, digital waveforms, thanks to specific signal coding, have spectral properties which are nearly independent of the signal content.

The most effective mathematical tool used for studying the radar performances of a given waveform is the ambiguity function (AF), mathematically defined as:

$$\left|\chi(\tau, f_d)\right|^2 = \left|\int_{-\infty}^{+\infty} s(t)s^*(t-\tau)\exp\left[j2\pi f_d t\right]dt\right|^2 \tag{1.1}$$

where $s(t)$ is the complex envelope of the transmitted signal, τ is the time delay and f_d is the Doppler frequency shift. The AF cross-section at $f_d = 0$ is the signal autocorrelation function (ACF).

By means of the ambiguity function, range and Doppler resolutions are directly obtained.

1.2. STATE OF THE ART

As a result of a study of the state of the art, some examples of passive radars are presented. The main characteristics dealing with antenna structure, receiving chains and processing architectures will be described.

1.2.1. PARADE (Passive Radar Demonstrator) Warsaw University of Technology

PaRaDe exploits transmissions from commercial FM radio stations in order to detect and track airborne targets [5],[6].

The antenna system is a circular antenna array composed of eight half-wave dipoles (Figure 1.2). Beamforming coefficients are applied for creating static beams, independently of the received signals. One beam is pointed in the transmitter direction, which is assumed to be known. The rest of beams correspond to the surveillance channels. The signal from each of the surveillance beams is fed to a separate processing chain (Figure 1.3).

The signal from the antennas is amplified, filtered and digitized in RF, without analog down conversion process. The selected radio channel is digitally down converted to the baseband by a quadrature demodulator and the complex IQ samples are sent to a general purpose PC using USB 2.0 interface. The software running on the PC is written in C/C++ and works under Windows or Linux operating systems. It consists of three parts responsible for: data reception, signal processing and visualization.

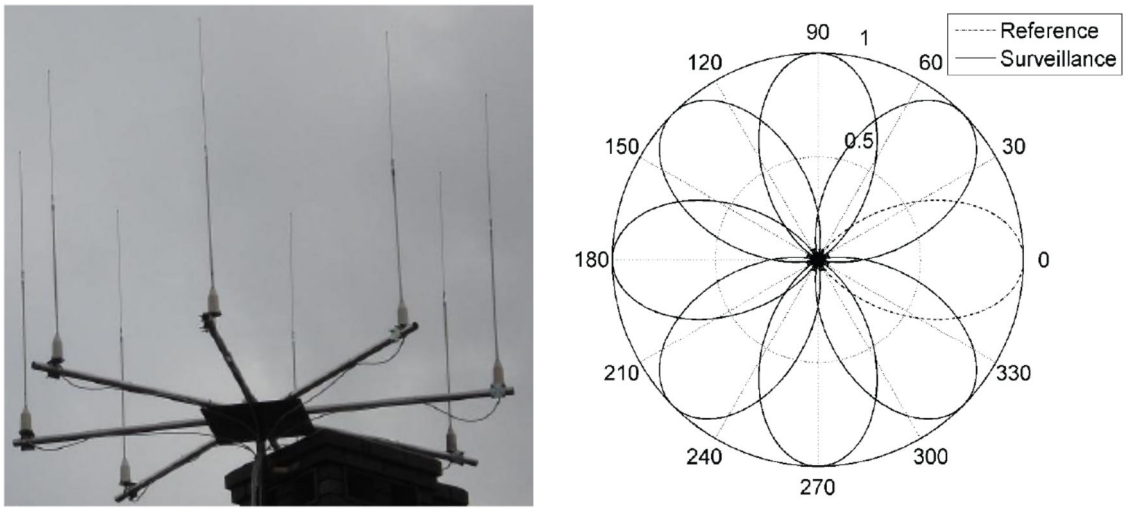

Figure 1.2 PaRaDe II: antenna array (left) and beam pattern (right)

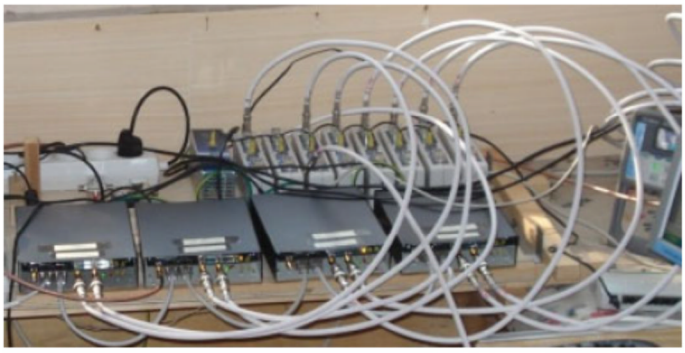

Figure 1.3 PaRaDe II: receiving chain

1.2.2. CORA COvert RAdar (FHR)

This system can exploit alternatively Digital Audio Broadcasting (DAB) or Digital Video Braodcasting-Terrestrial (DVB-T) signals, using a circular antenna array with elements for the VHF (150-350 MHz) and the UHF-range (400-700 MHz). A fiber optic link connects the elevated antenna and RF-frontend with the processing back-end, consisting of a cluster of high power 64 bit-processors [7],[12].

The array antenna (Figure 1.4) is composed by two 16 elements panels:

- The lower one is equipped with crossed butterfly dipoles for horizontal and vertical polarization, which cover the 150 to 350 MHz frequency range, for

DAB reception. The 16 elements, feeding the 16 receiver channels of the front-end, allow 360° beamforming.

- A half of the upper plane is equipped with 16 vertically polarized UHF-broad band dipoles for DVB-T reception, to allow for 180º beamforming. The other half of the upper plane is equipped with spare dipole elements.
- Alternatively, both planes can be equipped with crossed butterfly dipoles, which can be combined to sharpen the beam in elevation.

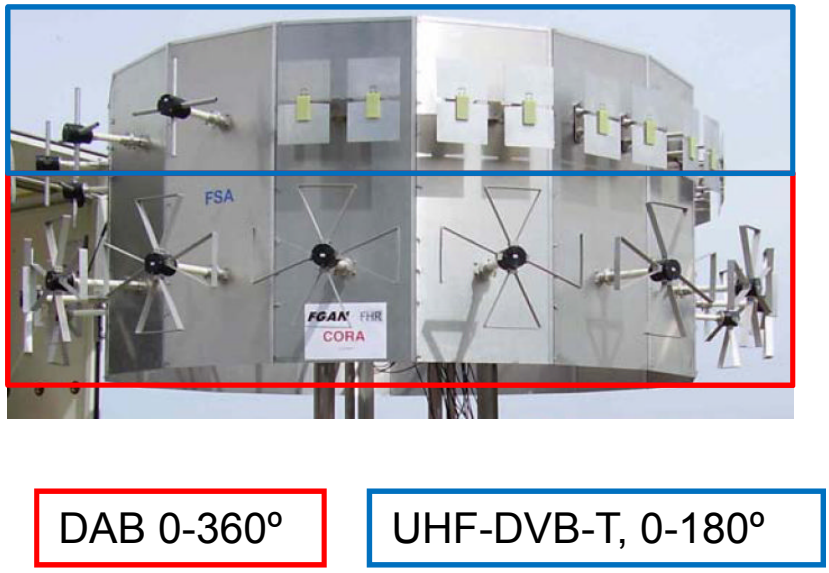

Figure 1.4 Cora antenna array: the lower panel is designed for DAB reception (red rectangle) and the upper one for DVB-T reception (blue rectangle).

The Cora system architecture is presented in Figure 1.5:

- The RF-front-end consists of 16 equal receiver channels, composed of a Low-Noise Amplifier (LNA), a tunable or fixed filter and an adaptive gain control for optimum control of the ADC.
- A chirp signal generated by a separate signal generator and transmitted to the front-end by coaxial cable, is used for calibration. A bank of switches provides for calibration of each receiver channel chain from the LNA to the ADC, excluding only the antenna element.

- A/D conversion is realized with 4 FPGA boards. Each boards is equipped with 4 ADC modules with 14 bit 100 Msamp/sec maximum sample rate ADC-chips, for processing 4 receiver channels. Each FPGA provide an output channel.
- Each ADC output is fed to an electro-optic converter and linked to the signal and data processing unit via a fiber-optic cable. In the signal and data processing unit, the optical signals are converted back to digital data streams of 4 serial channels, each, using 64-bit-boards, hosting 4 FPGAs. Four high performance Quad-Opteron computers handle the four data streams.

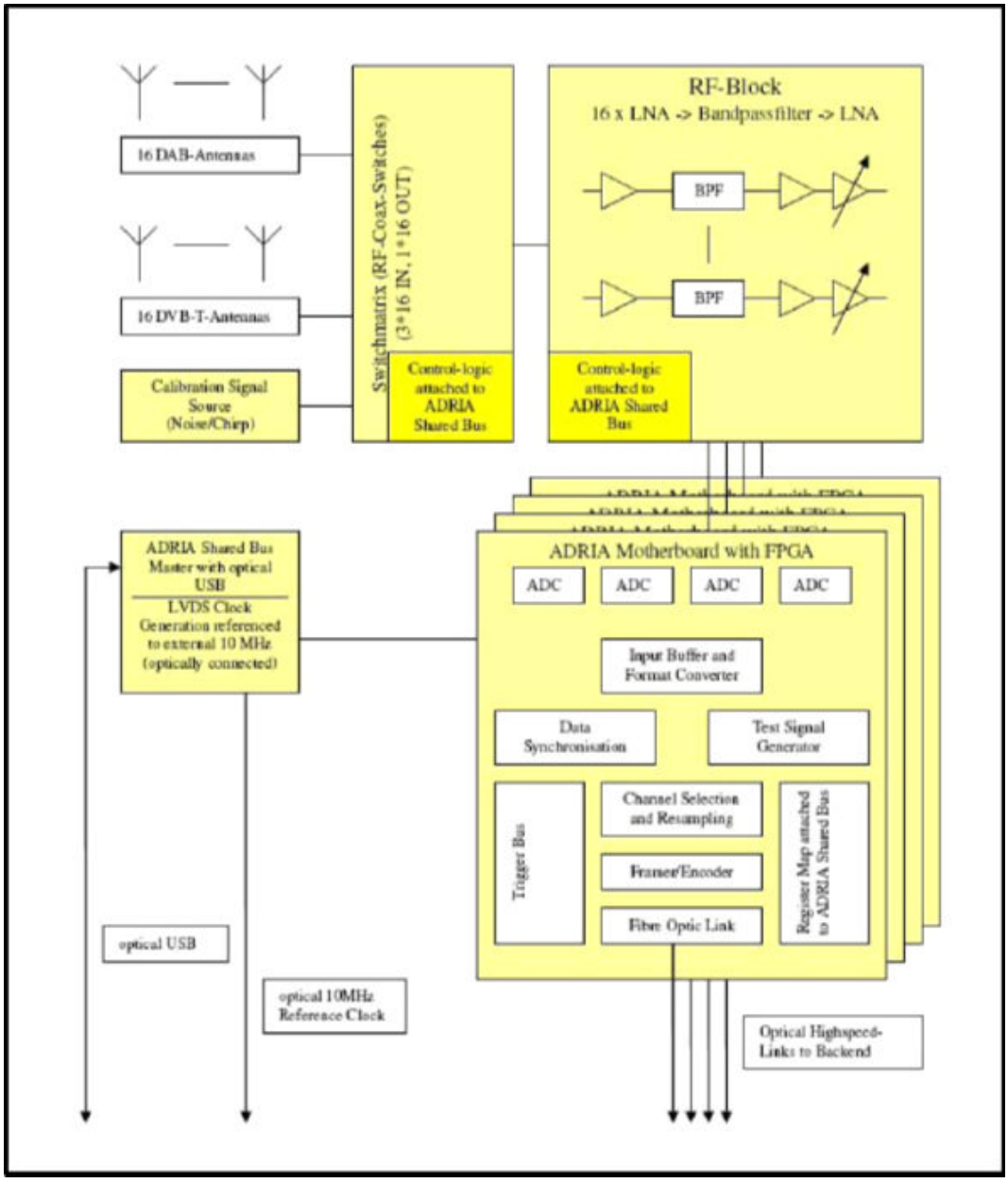

Figure 1.5 Cora system architecture

1.2.3. MULTIBAND Passive Radar Demonstrator, BAE System

This is a four-channel system capable of receiving and processing analogue and digital transmissions over a band covering 200MHz to 2GHz, providing sufficient bandwidth to process the analogue and digital transmissions of interest [13]. The system architecture is presented in Figure 1.6.

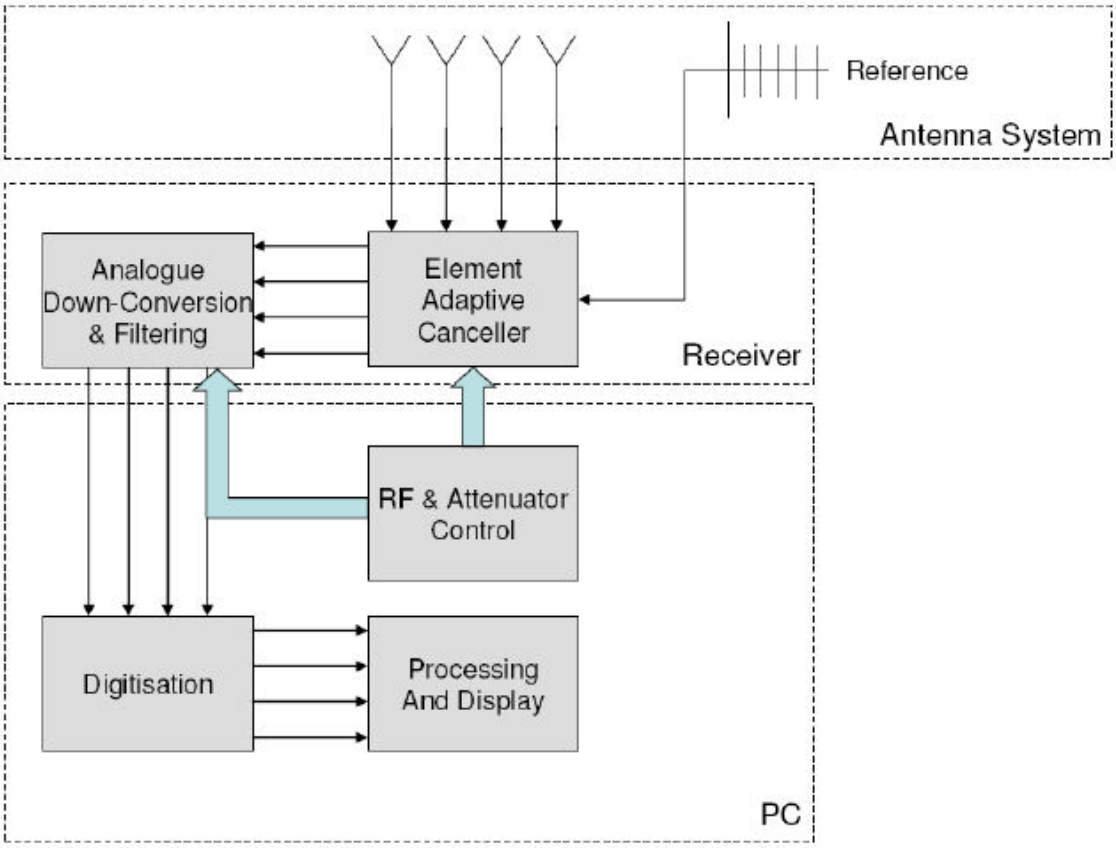

Figure 1.6 BAE system architecture

The antenna system consists of an array of four wideband Log-Periodic Dipole antennas, at a 45° angle from vertical to permit joint reception of vertically and horizontally polarized signals, with some loss. Additional, high gain, antennas were used for obtaining transmitter signal references.

The system incorporates near-instantaneous RF switching between one of several RF filters for true multiband system operation, under PC software control. The system was designed to operate on one of four channels. In the configuration reported in [13] a DAB channel and three DVB-T channels might be processed.

For reducing the DPI impact, analogue suppression of the direct signal at the element level was implemented. The reference signals were applied to vector modulators for obtaining anti-phase reference signals for addition to the main channel signals. The modulators were under PC control.

For data acquisition on a PC, an ICS-645-4A 32-bit 33MHz PCI card was selected. This provides four onboard ADCs clocked at up to 20MHz. A RAID array with dedicated raid controller card, multiple PCI buses, and enhanced data capture software enabled the required 80MB/sec (four channels at two bytes per channel and at 10MHz rate).

1.2.4. HOMELAND ALERTER 100 (THALES)

The Homeland Alerter 100 (Figure 1.7) is a passive radar sensor using illuminators of opportunity provided by FM radio broadcasts. Possible extension with DAB (Digital Audio Broadcast), AVB (Analog Video Broadcast) and DVB-T (Digital Video Broadcast –Terrestrial).

Figure 1.7 Homeland Alerter 100

The main characteristic of the system are :

- Detection performances on 360°:
- Range: class 100 km
- Elevation: 90°
- Ceiling: up to 20.000 ft * 24h/7 all weather surveillance

- Configurable for mobile platforms or fixed sites:
- Commercial or 4x4 military vehicle (using car driver licence)
- Stand alone or in network operations
- Connection to Command and Control Centers through Asterix/AWCIES protocol
- Delivered with a software (Aneth) for deployment support and performance prediction

The Homeland Alerter 100 has already been sold to several NATO countries.

1.2.5. AULOS (Passive Covert Location Radar) Selex Sistemi Integrati

In [4], the design, development and test of a Passive Covert Radar (PCR), exploiting a single non co-operative FM commercial radio station as its transmitter of opportunity are described. In Figure 1.8 the block diagram and the system are presented. The reference signal is collected by a single antenna. The surveillance system is composed of two antennas with independent receiving and processing chains. A "2/2 logic" is applied to extract the detections common to both channels, with ±1 cell tolerance in Doppler. Target bearing is estimated using a simple phase interferometry.

The receiver architecture is shown in Figure 1.9. In the analog section two down conversions are applied:

- The former lowers the carrier to the first IF and selects the FM channel of interest.
- The latter amplifies and moves the signal to the second IF.

This signal will be filtered, amplified and acquired by the A/D converter with 10 MSps clock frequency. Digital Down Conversion (DDC) is finally applied to obtain the complex signal digital components handled by signal and data processor.

The digital processing section, is running on three Intel® Core™2 PCs, connected via LAN.

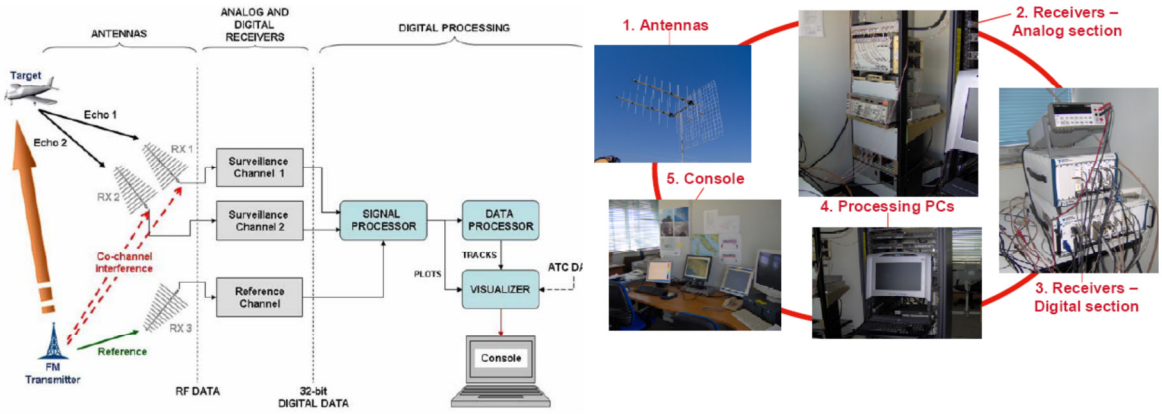

Figure 1.8 Aulos block diagram (left)and system (right)

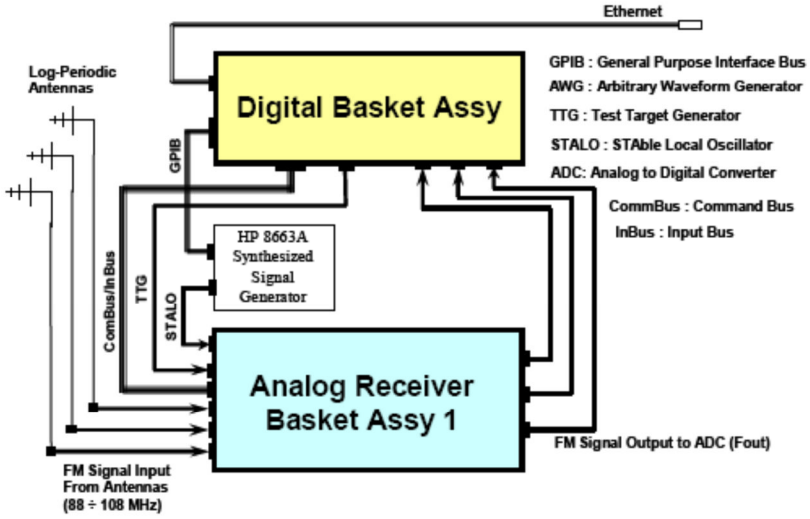

Figure 1.9 Aulos receiver architecture

1.2.6. SILENT SENTRY

The Silent SentryTM2 (SS2) system (Figure 1.10) is a receive system that exploits transmission from multiple commercial FM radio stations to passively detect and track airborne targets in real-time. On 10 May 1999,, Silent Sentry received Aviation Week & Space Technology magazine's Technology Innovation Award, which recognizes innovative product and service technologies in the global aerospace business.

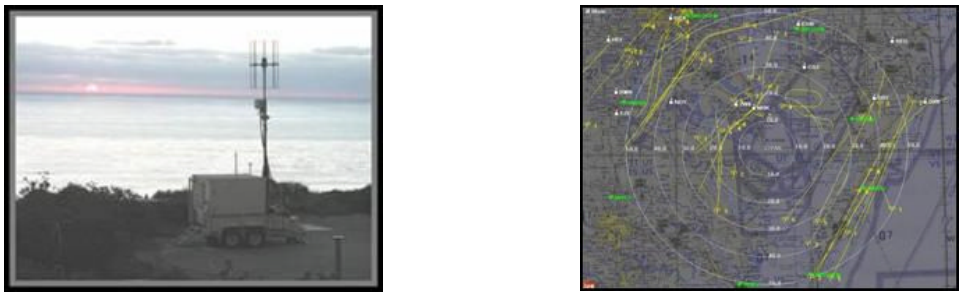

Figure 1.10 Silent Sentry system

Silent Sentry is a single receive system composed primarily of the following components the majority of which are commercial off-the shelf (COTS):

- **Target array:** a linear phased array for detecting the scattered energy from targets in the region of interest
- **Reference Antennas:** single element, identical to those in the target array, used for reception of the direct path signal from FM illuminators
- **High Dynamic Range Receivers:** accommodate the dynamic range requirements for receiving direct and scattered signals simultaneously.
- **A/D Converters:** the system possesses the capability to record data at this level, which is particularly useful for post-mission analysis
- **Processor:** Silicon Graphics, inc (SGI) general purpose processor
- **Displays:** SGI Octane workstations and visualizations products from the Autometric Edge Product Family™.
- **High Speed Tape System:** a SCSI attached striping tape controller with 5 tape drivers

Lockheed Martin currently has two configurations of SS2: the Fixes Site System (FSS) and the Rapid Deployment System (RDS).

1.2.7. CASSIDIAN MULTIBAND MOBILE Passive Radar System

In [14] a passive system capable of processing DVB-T SFN, DAB-SFN and 8 FM channels simultaneously is proposed. The architecture of the system is presented in Figure 1.11.. In this system, all the signals are digitally down converted according to the

software defined radio concept. The antenna system is depicted in Figure 1.12. It is composed of the following sub-systems:

- A 2x7 element planes covering the frequency band that ranges from 474 MHz to 850 MHz (DVB-T antenna), which allows 3D bearing.
- A 1x7 array covering the frequency range from 88 MHz to 240 MHz (FM/DAB signals), which allows 2D bearing.
- Auxiliary elements: a lightning, compass and calibration units.

In [14] only FM measurements are reported.

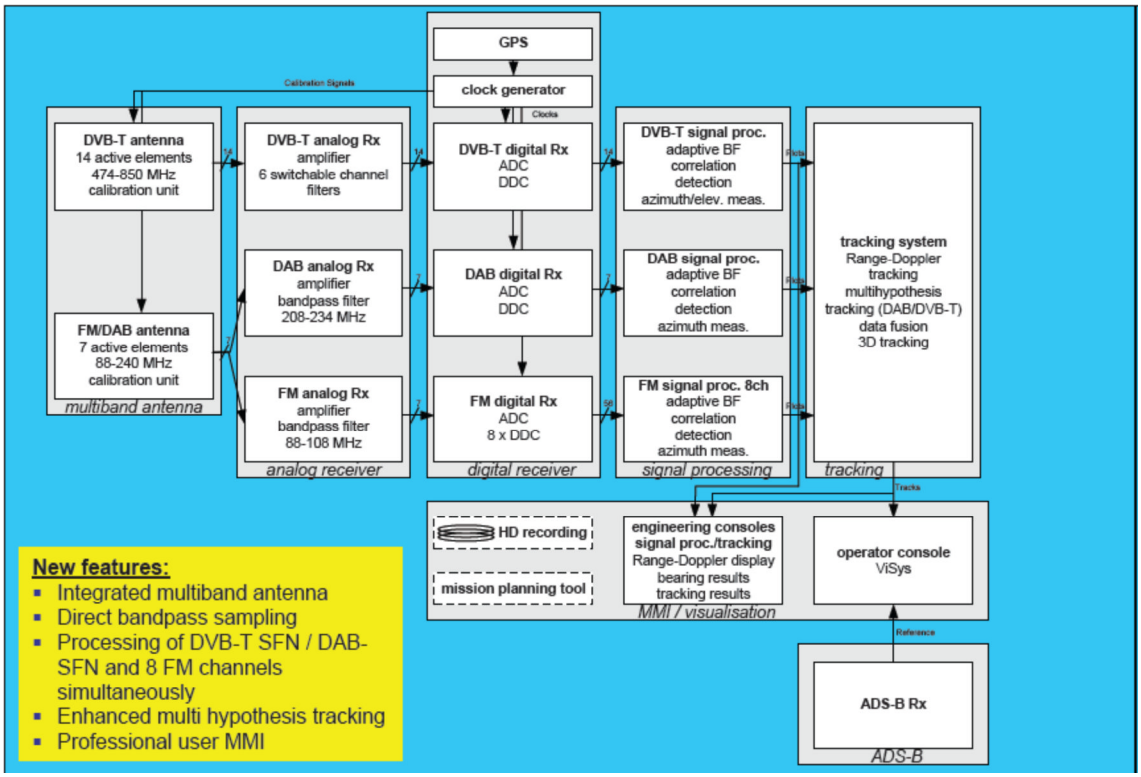

Figure 1.11 Cassidian system concept and architecture

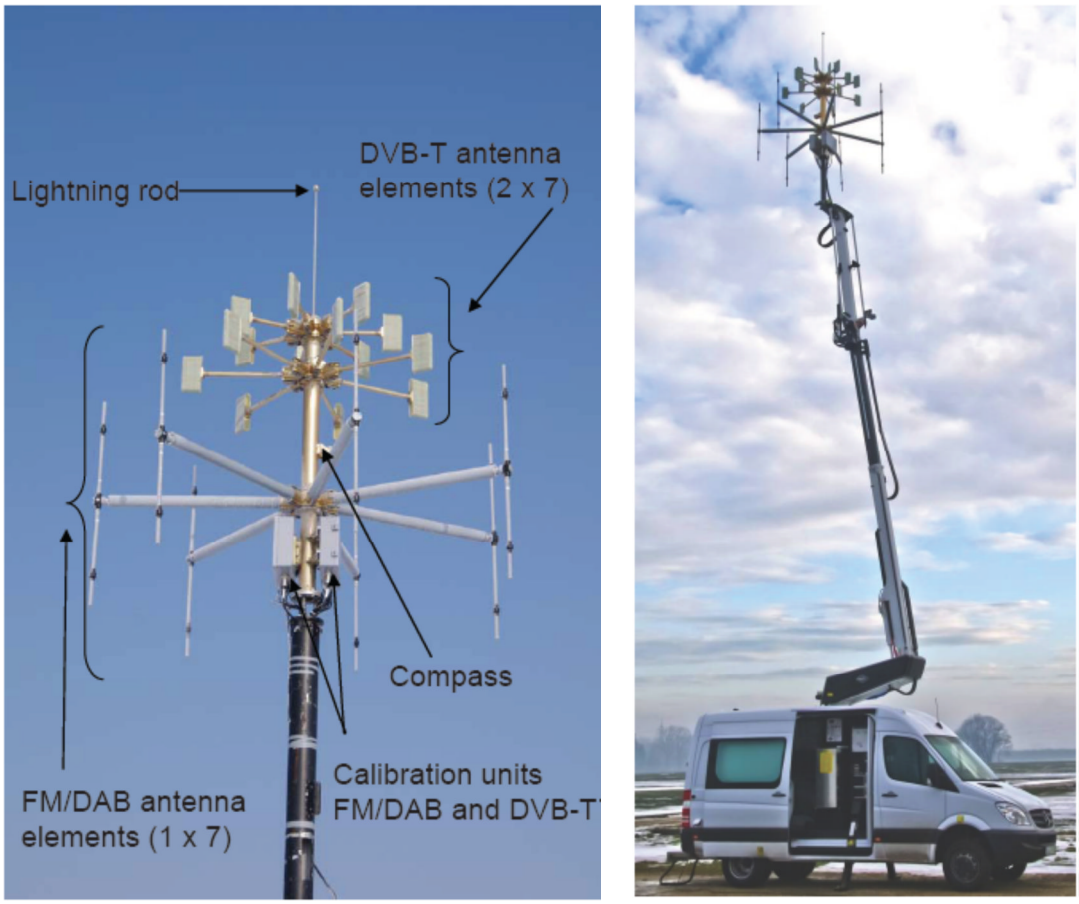

Figure 1.12 Cassidian system multiband antenna

1.3. BISTATIC RADAR

1.3.1. Bistatic radar Geometry

Figure 1.13 shows the bistatic geometry [15]. the transmitter and receiver are separeted by the baseline L. The angle subtended at the target by the transmitter and receiver is the bistatic angle, β . there are essentially three parameters that the bistatic receiver may measure:

I. The difference in Range $(R_T + R_R - L)$ between the direct signal and the transmitter-target-receiver path

II. The angle of arrival θ_R of the received echo

III. The Doppler shift f_d of the receive echo

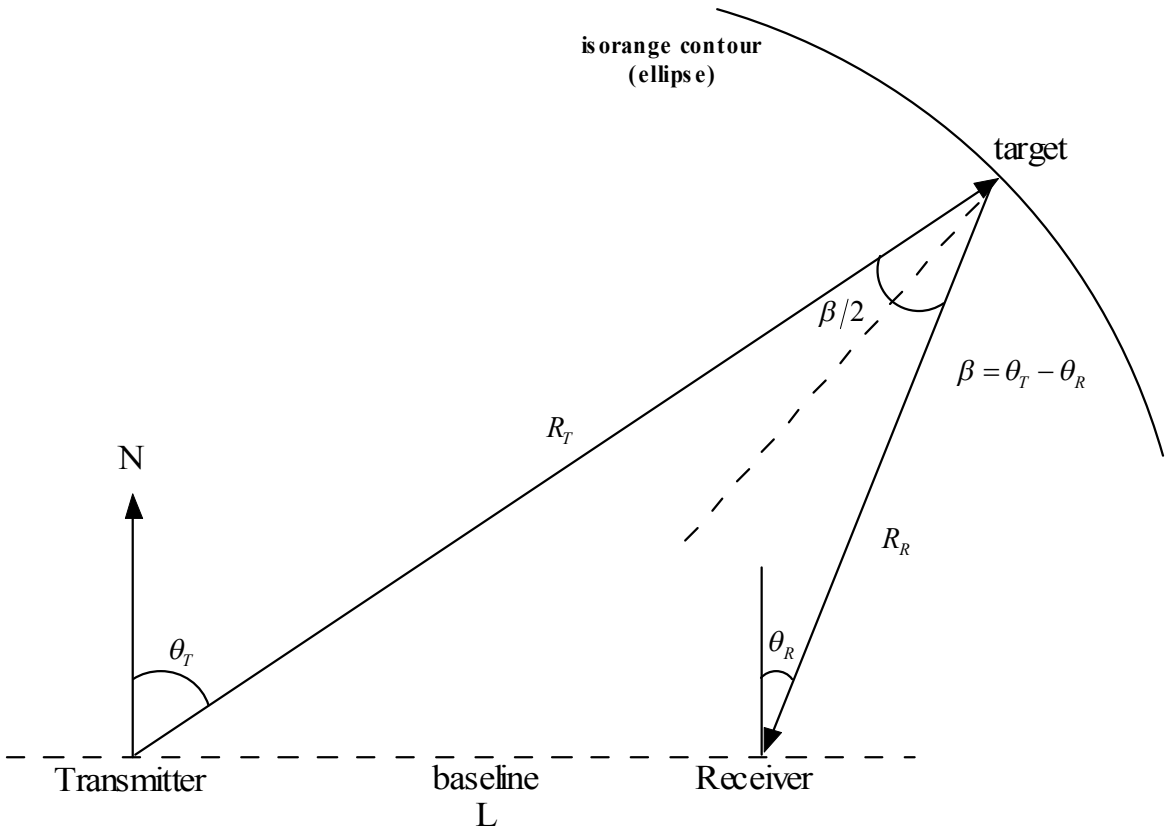

Figure 1.13 Bistatic radar geometry

Contours of constant bistatic range $(R_T + R_R)$ define an ellipse, with the transmitter and receiver at the two foci. If (R_T+R_R) and θ_R are measured and L is known, the range of the target from the receiver may be found from:

$$R_R = \frac{(R_T + R_R)^2 - L^2}{2(R_T + R_R + L\sin(\theta_R))} \tag{1.2}$$

In the general case when transmitter, target and receiver are all moving, the Doppler shift on the echo is obtain from the rate of change of the transmitter target receiver path. If the transmitter and receiver are stationary, the Doppler shift on the received echo is given by:

$$f_d = \frac{2v}{\lambda}\cos(\delta)\cos(\beta/2) \tag{1.3}$$

where v is the target velocity and δ is the angle of the velocity with respect to the bisector of the bistatic angle β .

1.3.2. Radar Equation

The starting point for prediction of PBR performance is the bistatic radar equation:

$$P_r = \frac{P_t G_t}{4\pi R_T^2}\cdot\sigma_b\cdot\frac{1}{4\pi R_R^2}\cdot\frac{G_r\lambda^2}{4\pi} \tag{1.4}$$

where

P_r is the receive signal power

P_t is the transmit power

G_t is the transmit antenna gain

R_T is the transmitter-to-target range

σ_b is the target bistatic radar cross-section

R_R is the target-to-receiver range

G_r is the receiver antenna gain

λ is the radar wavelength

The signal-to-noise ratio is obtained by dividing (1.4) by the receiver noise power $P_n = kT_0BF$ (where k is Boltzmann's constant, T_0 is 290 K, B is the receiver bandwidth and F the receiver noise figure), and multiplying by the receiver processing gain, also taking into account the various losses.

The factor $\left(\frac{1}{R_T^2 R_R^2}\right)$ in eq. (1.4) means that the signal-to-noise ratio has a minimum value for $R_T = R_R$, and is greatest when the target is either close to the transmitter or close to the receiver. Contours of constant values of $\left(\frac{1}{R_T^2 R_R^2}\right)$, and hence of signal-to-noise ratio, define geometric figures known as Ovals of Cassini [15].

In predicting the detection performance of a PBR system it is critical to understand the correct value of parameters to insert into this equation. In particular, it must be appreciated that the ambient noise level will be high, particularly in the VHF and UHF bands, and particularly in urban enjoinments, due the direct signal, co-channel signals, spectral 'slop', multipath, and noise. This means that dynamic range of PBR receiver will need to be substantial to cope with the wide range of the signal levels (typically >90dB)

1.4. TYPICAL ILLUMINATORS

Quite evidently, PBR depends upon the use of waveforms that are not explicitly designed for radar purpose. In Table 1.1, the main parameters of a number of different types of waveform are reported.

Signal of opportunity	Frequency (MHz)	EIRP (KW)	Instantaneous Bandwidth (MHZ)	Monostatic Range Resolution (m)
FM	87.5-108.0	250	0.16	937 (variable)
GSM	935-960 1805-1880	0.01-0.1	0.2	750
UMTS	2110-2170	0.001-0.1	3.84	39
DAB	174-240 1452-1490	0.8-1.6	1.536	100
DVB-T	164-860	0.1-10	7.61	19.7
Wi-Fi 802.11	2400	0.0001	5	30
Wi-MAX 802.16	2400	0.02	20	15

Table 1.1 Summary of typical parameters of PBR illuminator of opportunity

To summarize, there is a wide variety of different types of source that might be used for PBR purpose. The parameter that need to be taken into account in assessing their usefulness are:

I. their power density at the target
II. their coverage (both spatial and temporal)
III. the nature of their waveform

In general, digital modulation schemes are found to be more suitable than analog, since their ambiguity function properties are better (since the modulation is more noise-like), and they do not depend on the program material and they do not vary with time.

Among digital waveform the best compromise between range resolution and EIRP value can be achieved by using DVB-T signals.

In the next chapters we will show how a DVB-T based Passive Radar High Range Resolution can be achieved by jointly using adjacent multiple channels transmitted by the same IO.

1.5. PROCESSING CHAIN

A general block scheme of a passive radar system is sketched in Figure 1.14

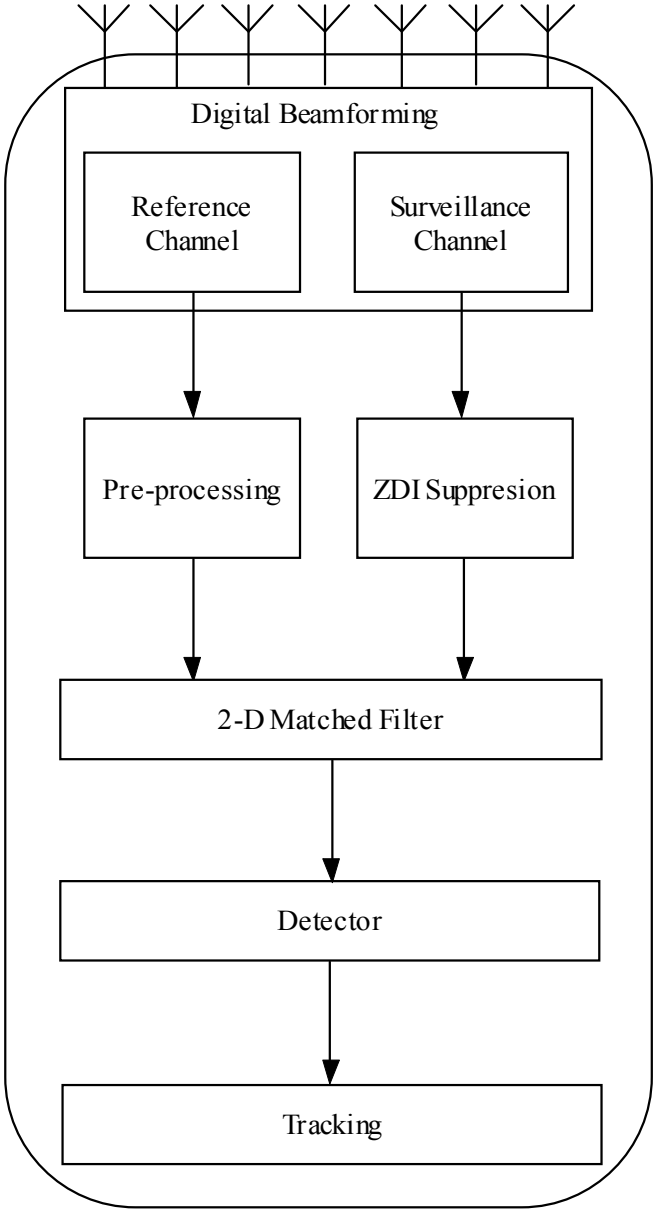

Figure 1.14 Signal Processing Chain for Passive Radar

A complete passive radar system typically consist of the following processing steps:

- **Digital Beamforming**: we can summarize the main goals of the digital beamforming in array passive radar as follow:
    - ✓ Reference channel beamforming: it is used to form the direct signal beams on the direction of the transmitters of opportunity that we intend to use for implementing passive radar functionality. Ideally the reference beam attempts to minimize the corruption in the transmitted waveform estimate caused by the superposition of unwanted signal multipath components.
    - ✓ Surveillance channel beamforming: it is used to form one or more surveillance beams in pre-determined directions selected for target search. Ideally the surveillance channel provides the maximum gain for target echoes while cancelling all interference components. A solution with multiple beams seems to be more practical since it provides higher gain and potential capability of the direction of the arrival estimations.
- **Pre-processing block**: it is used to remove spurious peaks of the radar ambiguity function caused by deterministic and pseudo-random pilot tones of the waveform
- **Zero Doppler Interference suppression**: is used to filter out the direct path interference, its multipath and the ground clutter, which are all characterized by a zero Doppler spectrum in the Range- Doppler domain
- **2-D Matched Filter**: it is used to generate the range- Doppler maps for each input channel, to determine target bistatic range and Doppler. This block represents the key processing step in a passive radar.
- **Detector**: it is used to detect targets in the 3D Range-Doppler -Azimuth (RDA) domain
- **Tracker**: it is used to reconstruct the path of targets in the 3D- RDA domain

In this thesis we developed only three signal processing blocks, specifically, Pre-processing, Zero Doppler Interference and 2D Matched Filter.

Chapter 2.

AMBIGUITY FUNCTION ANALYSIS

2.1. THEORETICAL BACKGROUND

Range and Doppler resolution are fundamentally important parameters in the design of any radar system as they govern the ability to distinguish between two or more targets by virtue of spatial or frequency (i.e. radial velocity) differences. The classical way of evaluating the behaviour of a waveform for radar purpose is the ambiguity function.

In PBR, and more generally in bistatic radar, the relative positions of target, transmitter and receiver govern the actual resolution that can be achieved. Here we used the formulation derived by Tsao et al. [16] to compute the bistatic ambiguity function:

$$\left|\chi\left(R_{RH},R_{Ra},V_H,V_a,\theta_R,L\right)\right|^2 = \tag{2.1}$$

$$= \left| \int_{-\infty}^{+\infty} s_t\left(t-\tau_a\left(R_{Ra},\theta_R,L\right)\right) s_t^*\left(t+\tau_R\left(R_{RH},\theta_R,L\right)\right) \times \right.$$
$$\left. \times \exp\left[j2\pi f_{DH}\left(R_{RH},V_H,\theta_R,L\right) - j2\pi f_{Da}\left(R_{Ra},V_a,\theta_R,L\right)t \right] dt \right|^2$$

where

- R_{RH} and R_{Ra} are the hypothesised and actual ranges (delays) from the receiver to the target
- V_H and V_a are the hypothesised and actual target radial velocities with respect to the receiver
- f_{DH} and f_{Da} are the hypothesised and actual Doppler frequencies
- θ_R and L as defined in Figure 1.13

The expression assumes the reference point of the PBR geometry to be the receiver, and is essentially a straight change of variables in eq. (1.1). The important difference is that the geometrical layout of the transmitter, receiver and target are now taken into account.

The ambiguity function can lose all range and Doppler resolution if a target is on or close to the transmitter-receiver baseline. for targets at long ranges the form of the ambiguity diagram is much like that for the monostatic case. These represent the two extremes, practical cases lie in between the two.

2.1.1. Bistatic Range Resolution

The bistatic range resolution can be calculated as the minimum distance between two targets that guarantees a time delay between their respective radar echoes equal to $c/2B$, where c is the velocity of light and B the signal bandwidth. In Figure 2.1 an example of a bistatic geometry is presented with three targets. Target 1 and Target 2 are collinear with the bistatic bisector, whereas target 3 present an aspect angle ψ. To generate $c/2B$ separation at a bistatic receiver, two point scattering targets, such as Targets1 and 2 in Figure 2.1, must lie on bistatic isorange contours having a separation, ΔR_B, that is approximately $c/\left(2B\cos\left(\beta/2\right)\right)$.

When a line joining the two targets is not collinear with the bistatic bisector, but at an aspect angle ψ with respect to the bistatic bisector, such as for Targets 1 and 3 in Figure 2.1, their physical separation ΔR_{ψ} must be approximately $\Delta R_B/\cos\left(\psi\right)$. Hence the expression that allows the calculus of this parameter is presented in (2.2) where β bistatic is the bistatic angle and ψ is the aspect angle with respect to the bistatic bisector [17]:

$$\Delta R \approx \frac{c}{2B\cos\left(\beta/2\right)\cos\left(\psi\right)} \tag{2.2}$$

The value obtained for $\psi = 0$ is usually used for specifying the bistatic range resolution of a system as a function of the bistatic angle.

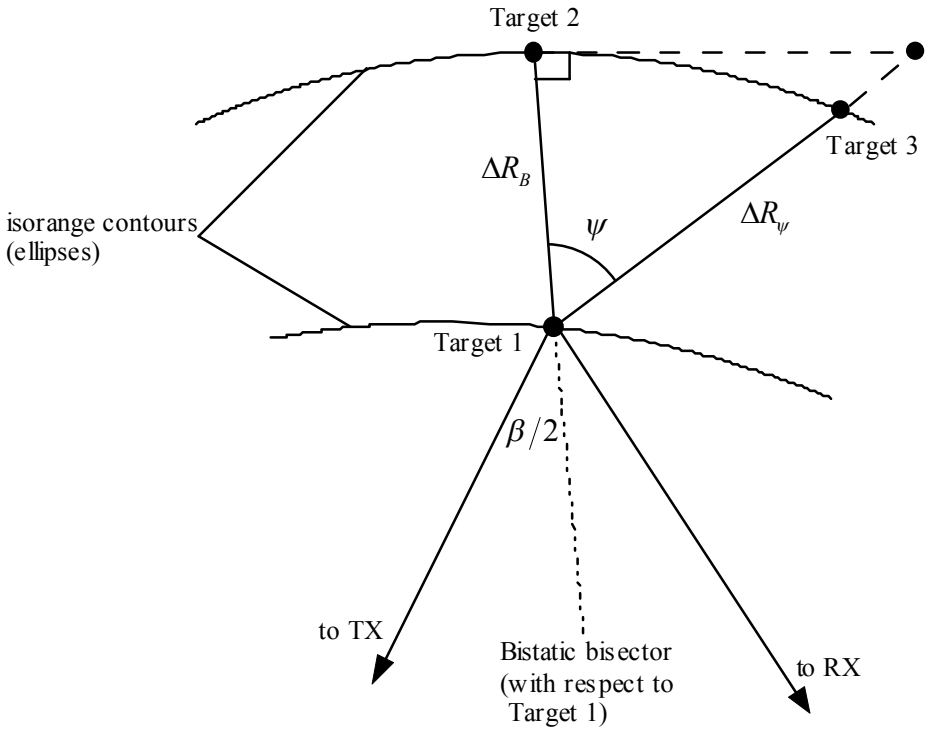

Figure 2.1 Geometry for bistatic range resolution

2.1.2. Bistatic Doppler Resolution

For monostatic and bistatic Doppler resolution, an adequate degree of Doppler separation between two targets echoes at the receiver is conventionally taken to be $1/T_{\text{int}}$ where T_{int} is the receiver's coherent processing interval. Thus the requirement for Doppler resolution is

$$\left| f_{Tgt1} - f_{Tgt2} = \frac{1}{T_{\text{int}}} \right| \tag{2.3}$$

where again, the equality represents a minimum requirement for Doppler separation. In the bistatic case the bistatic target Doppler is defined as

$$\begin{aligned} f_{Tgt1} &= \left(2V_1/\lambda\right)\cos\left(\delta_1\right)\cos\left(\beta/2\right) \\ f_{Tgt2} &= \left(2V_2/\lambda\right)\cos\left(\delta_2\right)\cos\left(\beta/2\right) \end{aligned} \tag{2.4}$$

The geometry for V_1, V_2, δ_1 e δ_2 is shown in Figure 2.2 . The two targets are assumed to be co-located so that they share a common bistatic sector. Combining (2.3) and (2.4) yields

$$\begin{aligned}\Delta V &= \left(V_1\cos\left(\delta_1\right) - V_2\cos\left(\delta_2\right)\right) = \\ &= \lambda \Big/ \left[2T_{\text{int}}\cos\left(\beta/2\right)\right]\end{aligned} \tag{2.5}$$

where ΔV is the required difference between the two target velocity vectors, projected onto the bistatic bisector, for adequate bistatic Doppler resolution. When $\beta = 0$, $\Delta V = \lambda \Big/ \left(2T_{\text{int}}\right)$, the monostatic case.

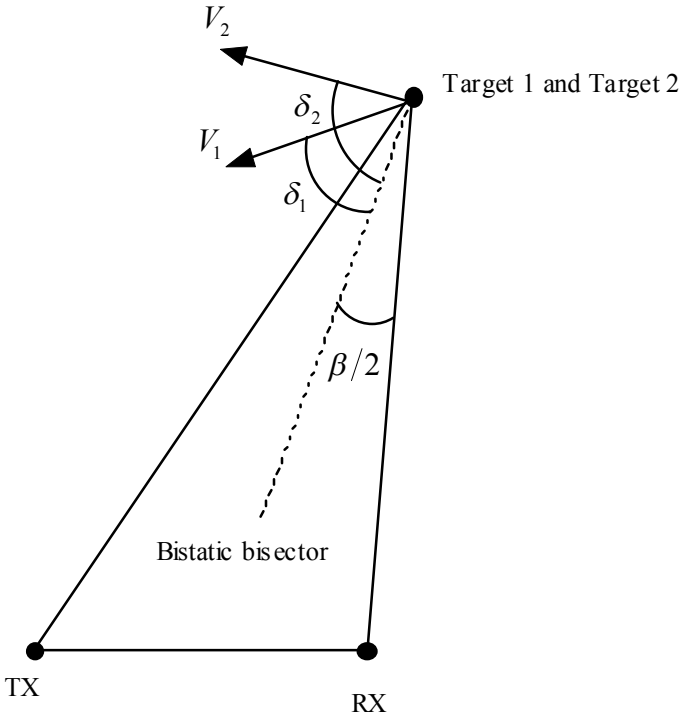

Figure 2.2 Geometry for bistatic Doppler resolution

2.2. DVB-T WAVEFORM ANALYSIS

Figure 2.3 shows the simplified block diagram of a DVB-T transmission system. The processing applied to the output transport stream of an MPEG-2 multiplexer consists of error coding interleaving and orthogonal frequency division multiplexing (OFDM). The combined processing is abbreviated as COFDM.

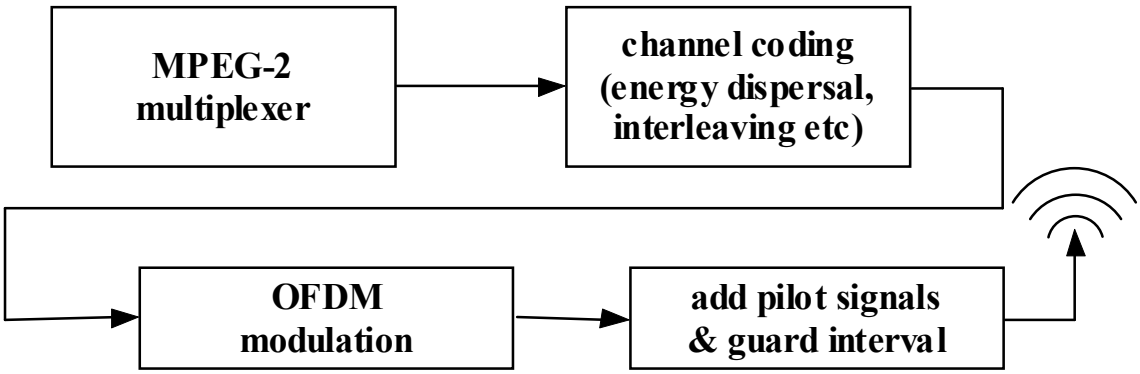

Figure 2.3 DVB-T transmission system

In OFDM, a wide frequency channel is divided into several sub-carriers that have relatively narrow frequency bandwidth (as shown in Figure 2.4).

The number of sub-carriers is important because the higher the number of sub-carriers spanning a fixed channel bandwidth, the narrower the spacing (bandwidth) of the sub-carriers. Hence, when 64 carriers are used in a 20 MHz channel, the sub-carrier spacing is 312.5 kHz, but when 2048 sub-carriers span the 20 MHz, the spacing is 15 kHz.

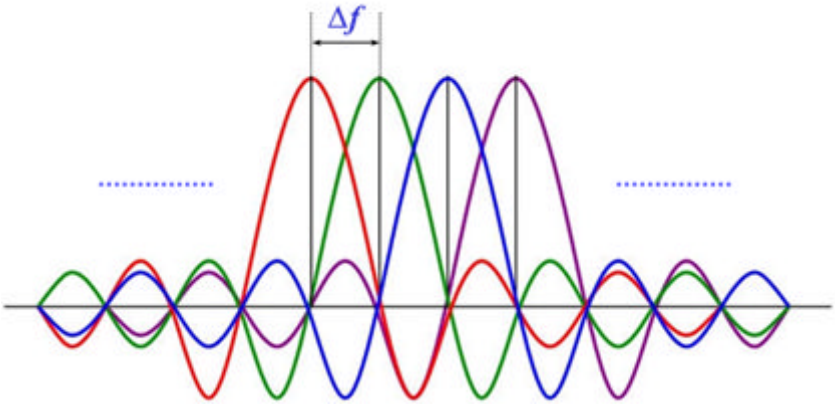

Figure 2.4 OFDM signal consists of several narrow sub-carriers

The sub-carrier spacing (or bandwidth) is important as the time domain OFDM symbol duration is the inverse of the sub-carrier spacing ($T_s = 1/\Delta f$). Hence, for the case of 64 carriers of 312.5 kHz, the symbols duration is $3.2\mu s$, whereas in the case of 2048 carriers of 15 kHz it is $66.7\mu s$.

The wireless propagation channel causes impairments to the transmitted signal. The width of the sub-carrier and duration of the OFDM symbol have direct role in mitigating these impairments. Long symbols and narrow sub-carriers are better suited for a channel that has long stability in time but varies quickly in the frequency domain whereas short symbols and wide sub-carriers are better suited for the case where the channel is highly varying in time yet relatively slowly changing in the frequency domain.

The DVB-T transmitted signal model is expressed in the following equation:

$$s(t) = \sum_{m=-\infty}^{+\infty} \sum_{k=0}^{N-1} c_k^{(m)} p(t - mT_S) \cdot e^{j2\pi k f_{SC} t} \tag{2.6}$$

The sub-carriers are separated by $f_{SC} = 1/T_s$ within the $B_{DVB-T} = 7.61MHz$ bandwidth. The number of sub-carriers depends on the implemented standard. In Italy, 6817 frequency sub-carriers $(T_s = 896\mu s)$ are used, where each sub-carrier is 16 or 64 QAM modulated with baseband data. The transmitted signal is organized in COFDM frames. Each frame consists of 68 OFDM symbols. Each symbol is formed by a set of data sub-carriers, pilots sub-carriers and transport parameter signalling (TPS).

The TPS carriers convey information about the parameters of the transmission scheme. The carrier locations are constant and defined by the standard and all carriers convey the same information using Differential Binary Phase Shift Keying (DBPSK). The initial symbol is derived from a Pseudorandom Binary Sequence (PRBS).

The pilot symbols aid the receiver in reception, demodulation, and decoding of the received signal. Two types of pilots are included: scattered pilots and continual pilots. The scattered pilots are uniformly spaced among the carriers in any given symbol. In contrast, the continual pilot signals occupy the same carrier consistently from symbol to symbol. The location of all pilot symbol carriers is defined by the DVB-T standard. Figure 2.5 illustrates the pilot spacing for a DVB-T OFDM frame where carriers are

indexed horizontally and symbols are indexed vertically [18]. The pilots are based on a PRBS and are BPSK modulated at a boosted power level, $16/9$ times greater than that used for the data and TPS symbols.

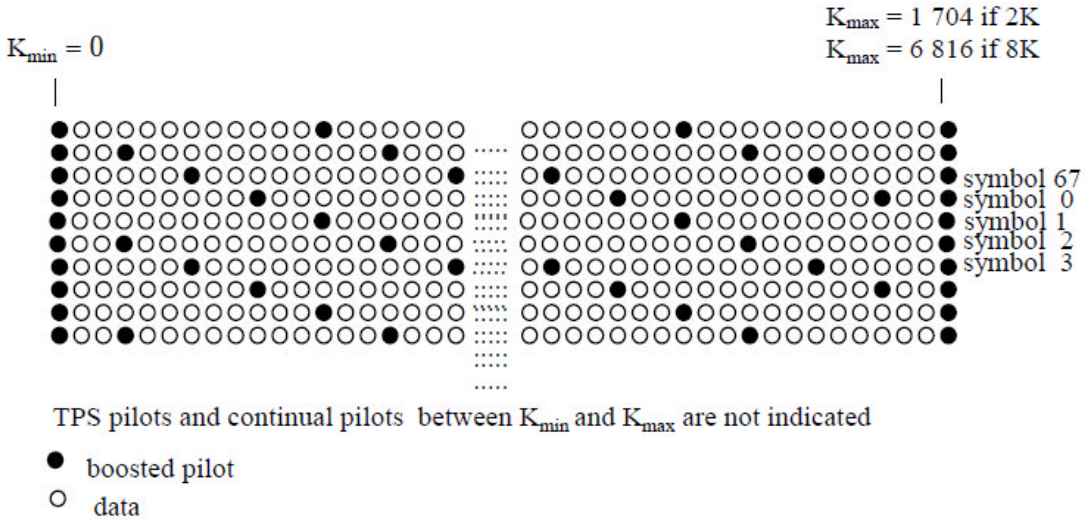

Figure 2.5 Pilot structure in the DVB-T OFDM frame

The COFDM symbol presents also a guard interval T_g also called the cyclic prefix, is added to make sure that the delayed symbols don't overlap with the following symbol. Otherwise, the delayed symbols will cause what's termed "inter-symbol interference," which is self-interference resulting from the effects of the propagation channel.

It is a segment of duration T_g, added at the beginning of the COFDM symbol.

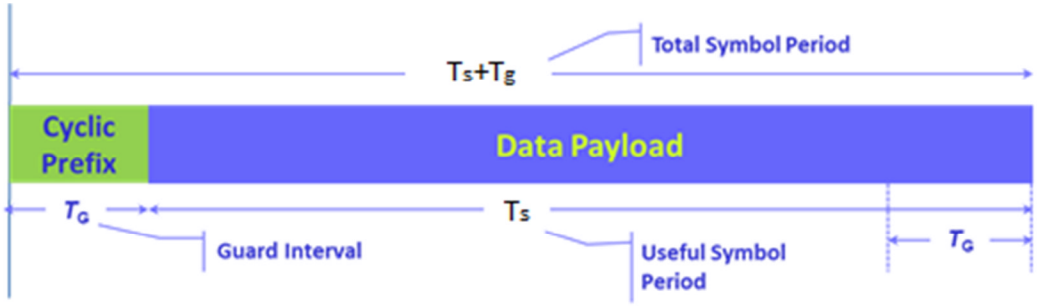

Figure 2.6 Guard Interval in OFDM symbol

This segment is identical to the segment of the same length at the end of the symbol. The duration of the guard interval ranges from 3% to 25% of T_s .

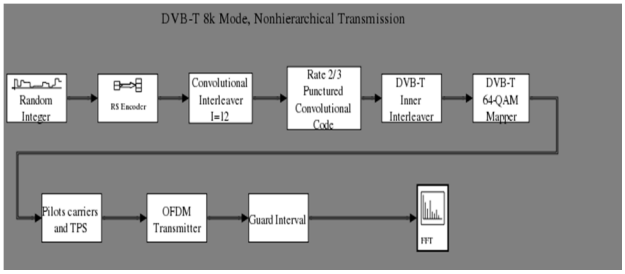

Figure 2.7 DVB-T simulator

A DVB-T transmission system has been simulated through a Simulink® model, see Figure 2.7. The spectrum of the DVB-T signal is a band-pass spectrum signal with a nearly rectangular envelop, as shown in Figure 2.8.

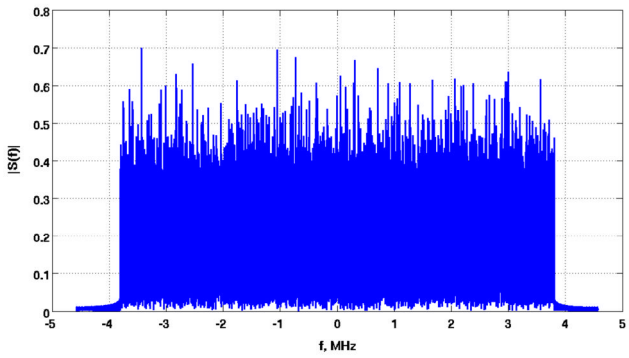

Figure 2.8 DVB-T spectrum

2.3. DVB-T AMBIGUITY FUNCTION ANALYSIS

The radar ambiguity function is a 2D autocorrelation function given by eq. (1.1).

An example from the simulation is given in Figure 2.9.

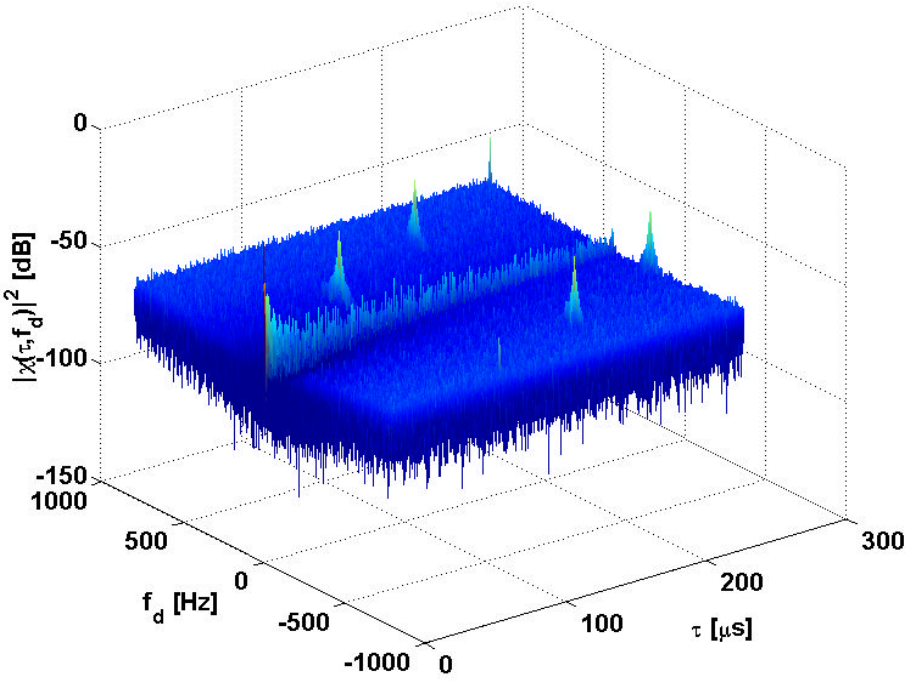

Figure 2.9 Ambiguity function of DVB-T signal

Several ambiguities are seen aside from the peak at zero-delay and zero-Doppler. To understand the source of these ambiguities, we must look more closely at the structure of the DVB-T signal, namely the pilot signals inserted into the OFDM structure.

The spacing of the scattered pilots is constant within a symbol. Scattered pilots are placed every twelve carriers. For the Italian 8k-mode DVB-T signal, this corresponds to 13.392 KHz $(12/T_s)$ and causes ambiguities to arise every $74.6\mu s$ $(T_s/12)$ in delay.

The scattered pilots are also spaced regularly across symbols. Every fourth symbol sees the scattered pilots occupying the same carrier (Figure 2.5). For the signal used, which has a guard interval (Δ/T_s) of $1/4$, this corresponds to scattered pilot spacing across symbols of $4.48ms$ and causes ambiguities to arise every $223.2Hz$ in Doppler. This is seen in Figure 2.9.

The next occurrence of ambiguity peaks is caused by the guard interval which is a

repeat of the end of the DVB-T symbol. This occurs at a delay of T_s. We also note that the power of these peaks is dependent on the length of the guard interval, but these are most likely outside of our processing scale.

2.4. MULTICHANNEL DVB-T AMBIGUITY FUNCTION ANALYSIS

A multichannel DVB-T signal can be analytically modelled as [19]:

$$s_{ref}(t) = \Re e\left\{\sum_{m=0}^{N_c-1} \tilde{s}_m(t) e^{j2\pi f_m t}\right\} \tag{2.7}$$

where N_C is the number of channels, f_m is the carrier frequency for the m-th channel and $\tilde{s}_m(t)$ is the complex envelope of the m-th channel. Under the assumption that the N_C channels are equally spaced, it is possible to write fm as $f_0 + m\Delta f$, where Δf represents the channel bandwidth. If $s_{ref}(t)$ is downconverted with respect to f_0, it is possible to write the complex envelope of the signal as:

$$\tilde{s}_{ref}(t) = \sum_{m=0}^{N_c-1} \tilde{s}_m(t) e^{j2\pi m\Delta f t} \tag{2.8}$$

The DVB-T multichannel ambiguity function (AF) of the signal $\tilde{s}_{ref}(t)$ can be written as:

$$\begin{aligned}\chi(\tau, f_d) &= \int_{-\infty}^{+\infty} \tilde{s}_{ref}(t)\tilde{s}_{ref}{}^{*}(t-\tau)e^{j2\pi f_d t}dt = \\ &= \sum_{m=0}^{N_c-1}\sum_{p=0}^{N_c-1}\int_{-\infty}^{+\infty} \tilde{s}_m(t)e^{j2\pi m\Delta f t}\tilde{s}_p{}^{*}(t-\tau)e^{-j2\pi p\Delta f(t-\tau)}e^{j2\pi f_d t}dt = \\ &= \sum_{m=0}^{N_c-1}\sum_{p=0}^{N_c-1} e^{j2\pi p\Delta f\tau}\int_{-\infty}^{+\infty} \tilde{s}_m(t)e^{j2\pi m\Delta f t}\tilde{s}_p{}^{*}(t-\tau)e^{-j2\pi p\Delta f t}e^{j2\pi f_d t}dt\end{aligned} \tag{2.9}$$

Under the following assumptions:

- $\tilde{s}_m(t)$ is a bandwidth-limited signal (with bandwidth equal to $2B$)
- the signal bandwidth is always smaller than the channel bandwidth, $\Delta f \geq 2B$ (i.e.: the channels do not overlap)

- the Doppler frequency is negligible with respect to the signal bandwidth, $f_d \ll 2B$

it is possible to rewrite eq.(2.9) as:

$$\chi(\tau, f_d) = \sum_{p=0}^{N_c-1} e^{j2\pi p\Delta f\tau} \int_{-\infty}^{+\infty} \tilde{s}_p(t)\tilde{s}_p{}^*(t-\tau)e^{j2\pi f_d t}dt = \sum_{p=0}^{N_c-1} e^{j2\pi p\Delta f\tau} AF_p(\tau, f_d) \tag{2.10}$$

where $AF_p(\tau, f_d)$ is the ambiguity function of a single DVB-T channel. Under the realistic assumption that the auto-ambiguity function of a generic single DVB-T channel exhibits the same main characteristics, eq.(2.10) can be simplified to:

$$|\chi(\tau, f_d)| \approx \left| AF(\tau, f_d) \sum_{p=0}^{N_c-1} e^{j2\pi p\Delta f\tau} \right| \approx \left| AF(\tau, f_d) N_c \frac{\text{sinc}(N_c\Delta f\tau)}{\text{sinc}(\Delta f\tau)} \right| \tag{2.11}$$

First of all, three adjacent DVB-T channels (Figure 2.10) have been simulated through a Simulink® model, then analysed and processed to obtain the AF of the DVB-T multichannel waveform.

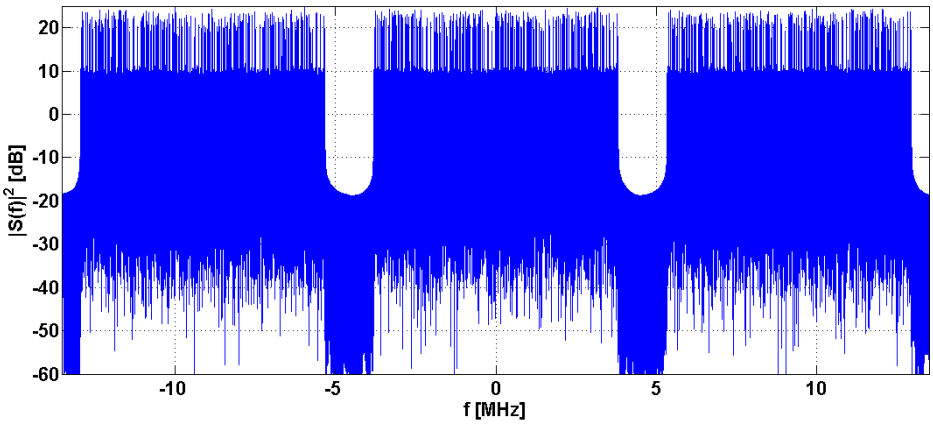

Figure 2.10 Multichannel DVB-T Spectrum

Multichannel DVB-T AF has the same shape of the single DVB-T AF as shown in Figure 2.11. Unwanted deterministic peaks in the AF are due to the known structure of the DVB-T signal, which includes pilots and guard intervals.

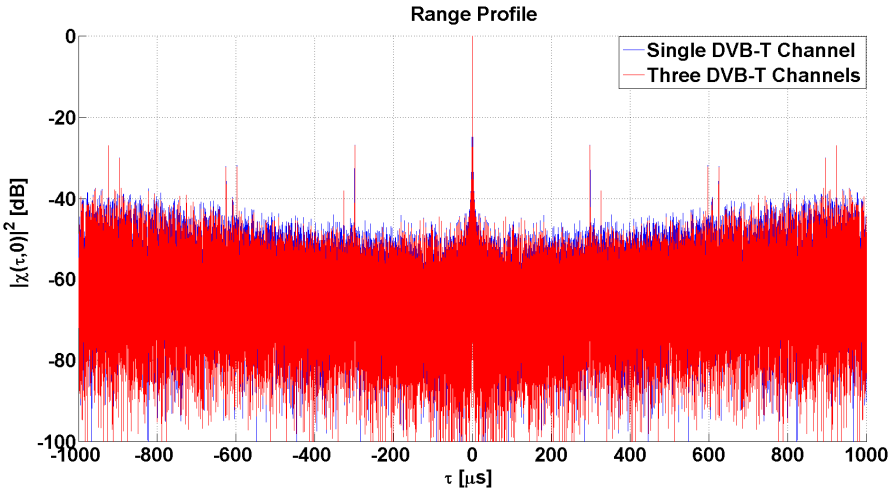

Figure 2.11 Single and Multichannel DVB-T Ambiguity Function

Specifically the single DVB-T channel ambiguity function is the envelope of multichannel DVB-T AF as confirmed by eq.(2.11) and the range resolution is improved a factor of N_C respect to the single DVB-T channel usage as shown in Figure 2.12. The side lobes present in the multichannel DVB-T AF due to the guard band between adjacent channels can be reduced by using windowing (Hamming, Kaiser, etc.).

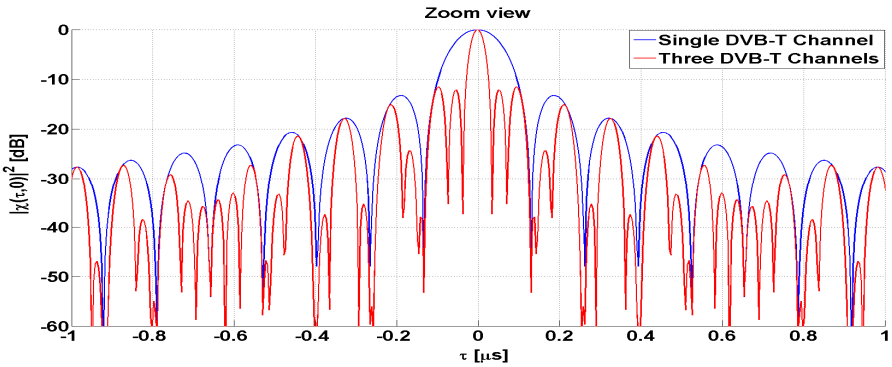

Figure 2.12 Single and Multichannel DVB-T Ambiguity Function (Zoom View)

2.5. REAL DATA AMBIGUITY FUNCTIONS

As a preliminary step, three adjacent DVB-T channels have been acquired through a SDR (Software Defined Radio) board, then analysed and processed to obtain the AF of the DVB-T multichannel waveform. The central frequency is 754 MHz and the whole analysed signal shows about 24 MHz of bandwidth Figure 2.13.

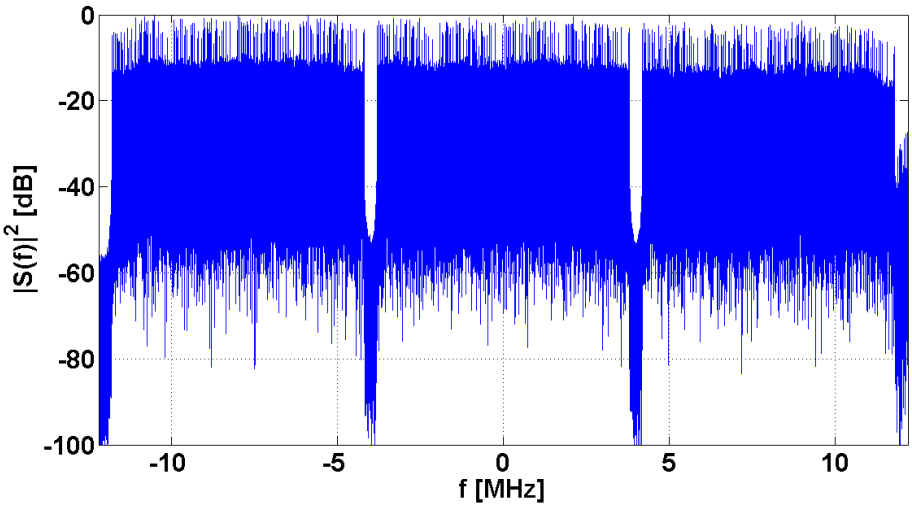

Figure 2.13 Multichannel DVB-T Spectrum: real data

Once again, the ambiguity function have been computed and compared with the one obtained for a single DVB-T channel. Plots of the ambiguity function along time delay (range) and Doppler frequency are represented in Figure 2.14. It is worth noting that the range resolution is improved by N_c times with respect to the single DVB-T channel, while the Doppler profile maintained the same behaviour.

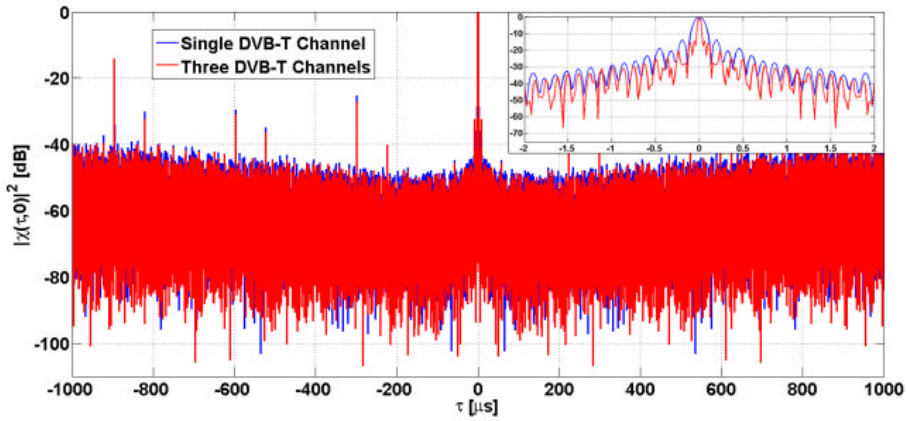

(a)

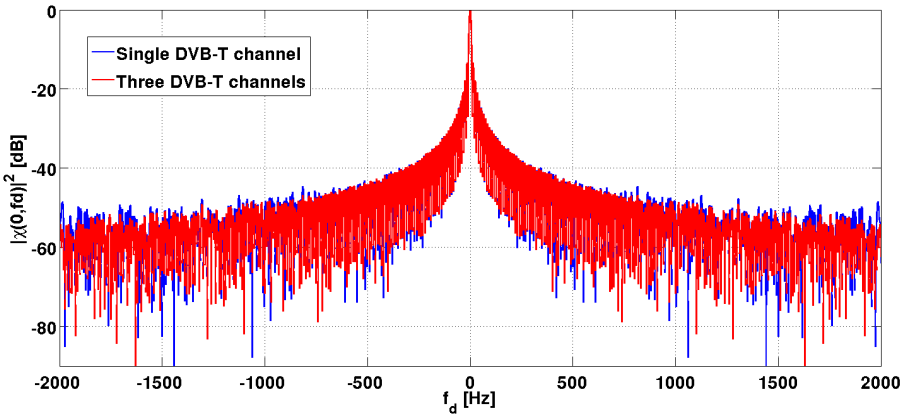

(b)

Figure 2.14 Multichannel AF from real data: a) Range profile: b) Doppler profile

The comparison between simulated and real data acquired with a low cost SDR architecture confirms the reliability of the DVB-T simulator.

Chapter 3.

PASSIVE RADAR SIGNAL PROCESSING WITH DVB-T SIGNAL

3.1. SINGLE DVB-T CHANNEL

3.1.1. DVB-T Pre-processing

The goal of this system is to filter the reference signal in order to resolve two problems:

- The multipath on the reference signal which can deteriorate the detection performance;
- Mitigate the effects of pilot carriers and guard interval on the ambiguity function of the signal.

For this reason this system can be divided in to two sub-system as reported in Figure 3.1

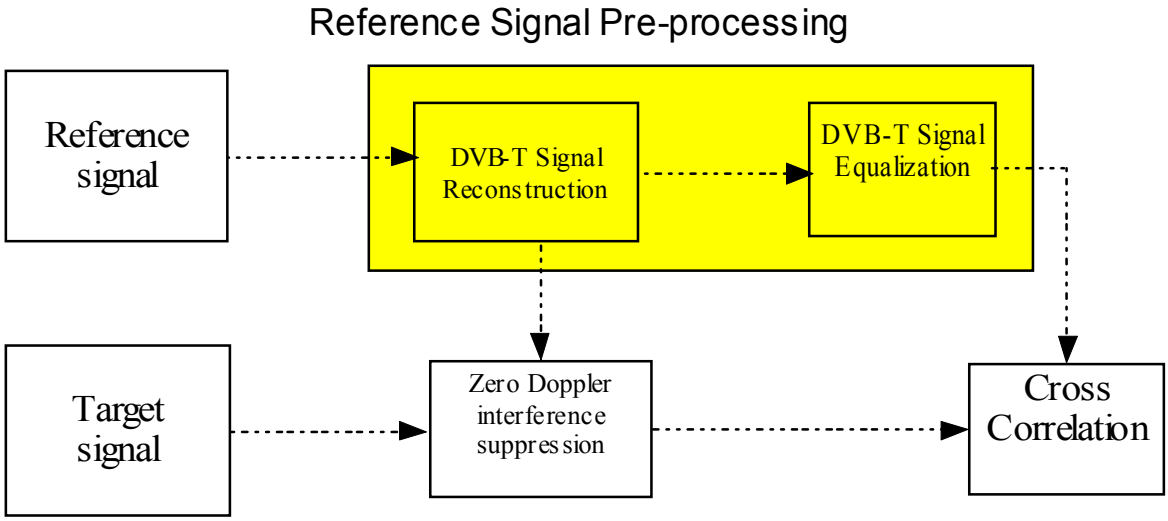

Figure 3.1 Reference Signal Pre-processing block

The DVB-T signal reconstruction and DVB-T Signal Equalization algorithms are described in the following paragraphs.

3.1.1.1. DVB-T Signal Reconstruction

In the reference channel, except for the presence of the thermal noise, the main degradation is due to the presence of multipath. When digital transmissions are exploited by a PBR, the multipath removal from the reference signal can be performed by demodulating the signal received at the reference antenna. A copy of the transmitted signal can be obtained by re-modulating the resulting symbol sequence according to the standard transmission [20].

A general block diagram of a DVB-T receiver is presented in Figure 4.21. The previous stages of Front End and Analog to Digital Converter (ADC) have not been represented.

Figure 3.2 General block diagram of a DVB-T receiver

- Pre-FFT synchronization: it represents a first coarse approach in the estimation of the carrier frequency offset and the timing shift. It estimates the time offset and the fractional carrier frequency offset, using the time domain signal by applying the autocorrelation to the Guard Interval (GI). At its output, the GI can be removed, before calculating the FFT.
- GI removal: the GI inserted at the beginning of every OFDM symbol is removed.
- FFT: the Fast Fourier Transform is applied.
- Post-FFT synchronization: it is based on two different stages. The first one is an acquisition stage, where the integer carrier frequency offset is estimated, and the second one is a tracking stage consisting of the estimation of the residual carrier frequency offset and the sampling frequency offset.

The correct location of each carrier within the received OFDM symbol can be determined. The received signal in frequency domain can thus be represented as

$$\begin{aligned} Y(k) &= \sum_{n=0}^{N-1} y(n) e^{\frac{-j2\pi kn}{N}}, \qquad n = 0,1,2,...N-1 \\ &= X(k) \cdot H(k) + W(k) \end{aligned} \tag{3.1}$$

where $H(k)$ denotes the channel transfer function of the channel and $W(k)$ noise contribution.

Extracting the pilot carrier contribution $Y(K_p)$ from the signal, the transfer function of the pilots is determined by

$$\hat{H}(l,k_p)=\frac{Y(l,k_p)}{X(l,k_p)}, \qquad k_p=1,2,...,N_p \tag{3.2}$$

where $X(l,k_p)$ denotes the well known pilot carrier

modulation in symbol l.

The channel characteristics for the remaining carriers can now be obtained with linear extrapolation. This algorithm uses the transfer functions from two successive pilot carriers k_p and k_p+1 to determine the channel response for the data carriers k_d in between.

Let L_d be the number of carriers between two pilots then the transfer function is given by

$$H(k)=\hat{H}(k_p)+\frac{d}{L_d}\left(\hat{H}(k_p+1)-\hat{H}(k_p)\right) \tag{3.3}$$

where $0\le d\le L_d$.

After the transfer function estimation, the information of the channel is used in order to equalize the OFDM symbol. In OFDM the equalization is simpler than traditional modulation because the information is carried within the frequency domain so that the equalization is only a subcarrier-wise multiplication by the equalization function. As with traditional systems two possible approach are presented: Zero-Forcing (ZF) and MMSE.

ZF approach in frequency domain simply tries to invert the channel. The equalization function $Q(l,k)$ is given by:

$$Q(l,k)=\frac{1}{\hat{H}(l,k)} \qquad k=0,1,2,...N-1 \tag{3.4}$$

The i-th equalized OFDM symbol $Z(l,k)$ is given by

$$Z(l,k) = Y(l,k) \cdot Q(l,k) = \frac{X(l,k) \cdot H(l,k)}{\hat{H}(l,k)} \qquad k = 0,1,2,...N\text{-}1 \tag{3.5}$$

With this equalization strategy, continual and scattered pilots are perfectly recovered in the equalized symbol and represents the milestones for the whole equalization[22].

ZF approach is the simplest way to equalize the signal but has some drawbacks. The most important one is the noise-enhancement. In fact, if the estimated value of the channel is low, when the channel inversion is imposed, the thermal noise can be enhanced. This effect can be shown by:

$$Z(l,k) = \frac{Y(l,k)}{\hat{H}(l,k)} = X(l,k) \cdot \frac{H(l,k)}{\hat{H}(l,k)} + \frac{W(l,k)}{\hat{H}(l,k)} \qquad k = 0,1,2,...N-1 \tag{3.6}$$

where the term $W(l,k)/\hat{H}(l,k)$ can reach high values and affects the correct de-mapping of the information $X(l,k)$.

In order to avoid this it is possibile to apply the MMSE approach which aims to find a function $Q(l,k)$ which minimizes the mean square error given by:

$$MSE = E\left\{\left|Z(l,k) - X(l,k)\right|^2\right\} = E\left\{\left|Y(l,k) \cdot Q(l,k) - X(l,k)\right|^2\right\} \tag{3.7}$$

The function $Q(l,k)$ can be written as:

$$Q(l,k) = \underset{Q(l,k)}{\arg\min}\, MSE = \frac{conj\left(\hat{H}(l,k)\right)}{\left|\hat{H}(l,k)\right|^2 + \hat{\sigma}_w^2} = \frac{1}{\hat{H}(l,k) + \dfrac{\hat{\sigma}_w^2}{conj\left(\hat{H}(l,k)\right)}} \tag{3.8}$$

where $H(l,k)$ is substituted by $\hat{H}(l,k)$ and σ_w^2 by $\hat{\sigma}_w^2$ which is the estimate noise power at the receiver.

MMSE equalization eliminates the noise-enhancement because the perfomance of the equalizer depends on the value of $\hat{H}(l,k)$. If $\hat{H}(l,k)$ is big, the first term prevails at the dominator and the equalizer acts as a ZF equalizer. If $\hat{H}(l,k)$ is small the second term prevails and this prevents the noise-enhancement. The drawback of this method is the need to estimate the noise power at the receiver.

3.1.1.2. DVB-T Signal Equalization

The specific structure of the DVB-T signal (par. 2.3), and specifically the presence of guard interval and pilot tones, introduces a number of undesired deterministic peaks in the AF which might yield significant masking effect on the useful signal and produces false alarm.

The technique proposed here exploits a filtering based on Least Squares (LS) method described in par. 3.1.2.

The goal of this technique is to find a vector of tap weights which minimize the sum of squared errors:

$$\min_{w} E(w) = \min_{w} \sum_{i=0}^{N-1} \left| e(i) \right|^2 \tag{3.9}$$

where w is the tap weight vector and $e(i)$ is defined as follows:

$$e(i) = S_{ref}(i) - \sum_{k=0}^{M-1} w_k^* S_{ref}(i - \tau_k) e^{j2\pi f_k i} \tag{3.10}$$

τ_k and f_k represents the position delay-Doppler of the k-th ambiguity.

Solving eq.(3.9) we obtain:

$$S_{ref_{FILT}} = S_{ref} - Zw^* = \left[I_N - Z\left(Z^H Z\right)^{-1} Z^H \right] S_{ref} = PS_{ref} \tag{3.11}$$

The matrix P projects S_{ref} signal composed by N samples in the subspace orthogonal to the interference subspace defined by $\underline{Z} = \left[\underline{P}\ \underline{\mathrm{N}}\right]$:

where $\underline{P}$ is define as:

$$\underline{P} = \begin{bmatrix} 0 & \dots & 0 \\ 0 & \dots & . \\ S_{ref}(1)\ \mathrm{e}^{j2\pi f_1 1} & \dots & . \\ S_{ref}(2)\mathrm{e}^{j2\pi f_1 2} & \dots & S_{ref}(1)\ \mathrm{e}^{j2\pi f_p 1} \\ S_{ref}(3)\mathrm{e}^{j2\pi f_1 3} & \dots & S_{ref}(2)\mathrm{e}^{j2\pi f_p 2} \\ . & \dots & . \\ . & \dots & . \\ S_{ref}(N-2)\mathrm{e}^{j2\pi f_1 N} & \dots & S_{ref}(N-\tau_{kp})\mathrm{e}^{j2\pi f_p N} \end{bmatrix} \quad p = 1, 2.....N_{kp} \tag{3.12}$$

where τ_{kp} represents positive range bin ambiguities and N_{kp} the number of positive ambiguities.

Instead $\underline{\mathrm{N}}$ is defined as:

$$\underline{N} = \begin{bmatrix} S_{ref}(2)\ \mathrm{e}^{j2\pi f_1 2} & \dots & S_{ref}(-\tau_{kn})\ \mathrm{e}^{-j2\pi f_k \tau_{kn}} \\ S_{ref}(3)\mathrm{e}^{j2\pi f_1 3} & \dots & S_{ref}(-\tau_{kn}+1)\mathrm{e}^{-j2\pi f_k \tau_{kn}} \\ . & \dots & . \\ . & \dots & . \\ . & \dots & S_{ref}(N)\mathrm{e}^{j2\pi f_k N} \\ S_{ref}(N)\mathrm{e}^{j2\pi f_1 N} & \dots & . \\ 0 & \dots & . \\ 0 & \dots & 0 \end{bmatrix} \quad k = 1, ...N_{kn} \tag{3.13}$$

where τ_{kn} represents negative range bin ambiguities and N_{kn}. the number of negative ambiguities.

For the purpose of our analysis, the reference and surveillance antennas are assumed to be co-located with the reference antenna steered toward the transmitter and the surveillance antenna pointed in the direction to be surveyed.

The complex envelope of the signal at the reference channel is:

$$S_{ref}(t) = S_T(t) + W_T(t) \tag{3.14}$$

where $S_T(t)$ is the complex envelope of the transmitted signal and $W_T(t)$ is the thermal noise contribution. The complex envelope of the target signal in the surveillance channel is given by:

$$S_{Surv}(t) = S_T(t-\tau)e^{j2\pi f_D t} + W_{Surv}(t) \tag{3.15}$$

The detection process in passive radar is based on the evaluation of the delay-Doppler cross-correlation function between the surveillance and the reference signal:

$$s_{ref} \otimes s_{surv} = AF(\tau, f_D) = \int_0^{T_{\text{int}}} s_{ref}^*(t-\tau)\, s_{surv}(t)\, e^{-j2\pi f_D t} dt \tag{3.16}$$

The reference signal after the equalization become:

$$S_{ref_{FILT}} = S_{ref}(t) - \hat{w}_1^* S_{ref}\left(t-\tau_{1\,amb}\right)e^{j2\pi f_1 t} - \hat{w}_2^* S_{ref}\left(t+\tau_{2\,amb}\right)e^{j2\pi f_2 t} \tag{3.17}$$

substituting eq. (3.15) into eq. (3.17) we obtain:

$$\begin{aligned} &S_{ref_{FILT}} = S_T(t) + W_T(t) - \hat{w}_1^* S_T\left(t-\tau_{1\,amb}\right)e^{j2\pi f_1 t} - \hat{w}_1^* W_T\left(t-\tau_{1\,amb}\right)e^{j2\pi f_1 t} \ldots \\ &\ldots - \hat{w}_2^* S_T\left(t+\tau_{2\,amb}\right)e^{j2\pi f_2 t} - \hat{w}_2^* W_T\left(t+\tau_{2\,amb}\right)e^{j2\pi f_2 t} \end{aligned} \tag{3.18}$$

It is worth noting that the number of ambiguities (in this case two) may vary according to the type of IO.

The 2D-CCF evaluated at the output of the equalization filter therefore becomes:

$$\begin{aligned} &S_{ref_{FILT}} \otimes S_{Surv}(t) = AF(\tau, f_D) + S_T(t) \otimes W_{Surv} + W_T(t) \otimes S_T(t-\tau)e^{j2\pi f_D t} + \ldots \\ &\ldots W_T(t) \otimes W_{Surv}(t) - \hat{w}_1^* AF\left(\tau-\tau_{1\,amb}, f_D - f_1\right) - \hat{w}_1^* S_T\left(t-\tau_{1\,amb}\right)e^{j2\pi f_1 t} \otimes W_{Surv}(t) - \ldots \\ &\ldots \hat{w}_1^* W_T\left(t-\tau_{1\,amb}\right)e^{j2\pi f_1 t} \otimes S_T(t-\tau)e^{j2\pi f_D t} - \hat{w}_1^* W_T\left(t-\tau_{1\,amb}\right)e^{j2\pi f_1 t} \otimes W_{Surv}(t) - \ldots \\ &-\hat{w}_2^* AF\left(\tau+\tau_{2\,amb}, f_D - f_2\right) - \hat{w}_1^* S_T\left(t+\tau_{2\,amb}\right)e^{j2\pi f_2 t} \otimes W_{Surv}(t) - \ldots \\ &\ldots \hat{w}_2^* W_T\left(t+\tau_{2\,amb}\right)e^{j2\pi f_2 t} \otimes S_T(t-\tau)e^{j2\pi f_D t} - \hat{w}_2^* W_T\left(t-\tau_{2\,amb}\right)e^{j2\pi f_2 t} \otimes W_{Surv}(t) \end{aligned} \tag{3.19}$$

If we merge the noise components we obtain:

$$\begin{aligned} &S_{ref_{FILT}} \otimes S_{Surv}(t) = AF(\tau, f_D) - \hat{w}_1^* AF\left(\tau-\tau_{1\,amb}, f_D - f_1\right) - \ldots \\ &\ldots \hat{w}_2^* AF\left(\tau+\tau_{2\,amb}, f_D - f_2\right) + N(t) \end{aligned} \tag{3.20}$$

We can observe three components, the ambiguity function centered around the target delay and two contributions which cancel the ambiguities (in this case two) due to the target.

3.1.2. Zero Doppler Interferences suppression

As is intrinsic in the passive radar concept, that involves the parasitic exploitation of an existing transmitter of opportunity, the characteristics of the transmitted waveform are not under control of the radar designer and they are not tailored for radar application. The goal of this processing block is to suppress all the interference located at zero Doppler namely the residual direct signal and its multipath, as well as ground clutter [21] (returns from the surround ground area where the target is located).

The proposed method is named Least Squares (LS). In computational terms, the least square algorithm is a batch processing approach [23].

The input data stream is arranged in a block of equal length, and the filtering of the input data is processed on a block by block basis as shown in Figure 3.3.

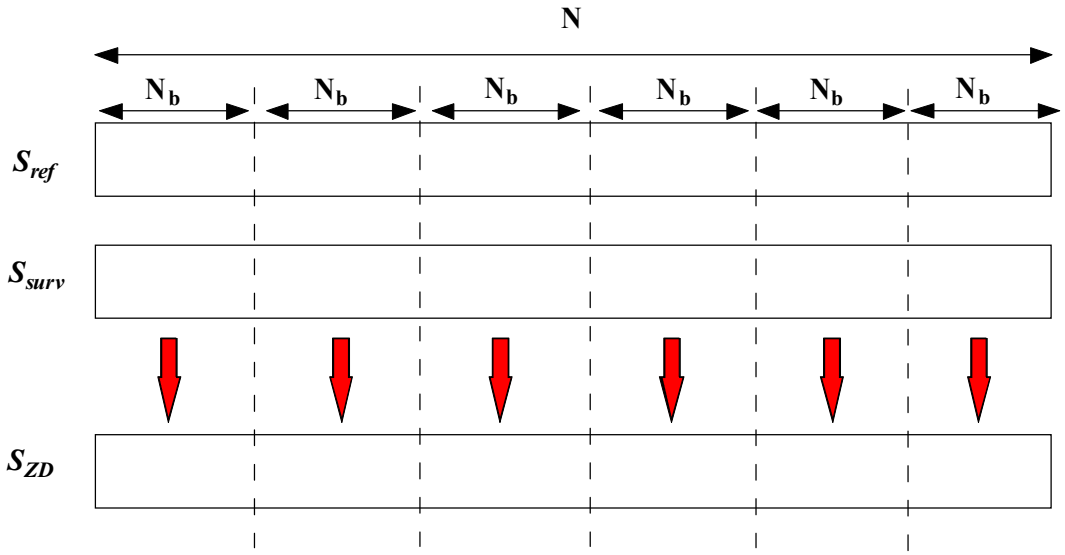

Figure 3.3 Sketch of LS batches algorithm

To derive the basic block LS algorithm, we consider the transversal filter structure, denoted by S_{surv} a vector composed by N samples of the received signal $S(n)$, and let S_{ref} be a vector composed by $N+M-1$ samples of the reference signal $S_{ref}(n)$. The goal of the LS method is to find a vector of tap weights which minimize the sum of squared errors as reported in eq.(3.9) where w is the tap weight vector and $e(i)$ is defined as follows:

$$e(i) = S_r(i) - \sum_{k=0}^{M-1} w_k^* S_{ref}(i-k) \tag{3.21}$$

Reformulating eq.(3.21) in terms of data matrix, we have:

$$e = S_r - Xw^* \tag{3.22}$$

so that eq. (3.9) becomes:

$$\min_w E(w) = \min_w \|e\|^2 = \min_w \left\{ \left\| S_r - Xw^* \right\|^2 \right\} \tag{3.23}$$

where

$$X = \begin{bmatrix} S_{ref}(1) & 0 & 0 & \cdots & 0 \\ S_{ref}(2) & S_{ref}(1) & 0 & & \\ \cdot & S_{ref}(2) & S_{ref}(1) & & \\ \cdot & \cdot & \cdot & & \\ \cdot & \cdot & \cdot & & \\ S_{ref}(N_b) & S_{ref}(N_b-1) & S_{ref}(N_b-2) & \cdots & S_{ref}(N_b-M+1) \end{bmatrix} \tag{3.24}$$

The columns of X define a basis for M-dimensional clutter subspace, where M is the number of the first range bins. We may solve eq.(3.23) by expressing the tap weight vector as:

$$w^* = (X^H X)^{-1} X^H S_r \tag{3.25}$$

Using eq.(3.22) and eq.(3.25)

$$S_{ZD} = S_{Surv} - Xw^* = \left[I_N - X\left(X^H X\right)^{-1} X^H \right] S_{Surv} = PS_{surv} \tag{3.26}$$

We may view the multiple matrix product $X\left(X^H X\right)^{-1} X^H$ as a projection operator onto a linear space spanned by the rows of data matrix X that represents the clutter subspace.

On the contrary P projects the received vector S_{surv} in the subspace orthogonal to the clutter subspace. The error vector S_{ZD} is the received signal with zero-Doppler components attenuated.

3.1.3. 2-D Matched Filter

The goal of this block is to implement an effective algorithm to cross-correlate the reference signal with the surveillance signal in order to reconstruct the Range-Doppler map (the Cross-Ambiguity function) [24]. The analytical expression of the cross correlation is given by:

$$\chi(\tau, f_d) = \int_0^{T_{int}} s_{ref}^*(t-\tau_m)\, s_{surv}(t)\, e^{-j2\pi f dt} dt \tag{3.27}$$

where f_d and τ are the Doppler frequency and time delay, respectively, while T_{int} is the integration time and S_{ref} is the reference signal.

In terms of computational burden, the CAF is one of the most heavy signal processing operations in a passive radar signal chain. As a matter of fact, long integration times (LIT) are required to obtain a proper level of signal to noise ratio (SNR). Moreover, the dimensions of the time- Doppler map depend on the maximum time delay (or maximum range) and maximum Doppler frequency (or velocity).

The reference signal $x_{ref}(t)$ can be seen as the sum of n_B contiguous batches of length T_B and it can be written as

$$x_{ref}(t) = \sum_{i=0}^{n_B-1} x_i(t - iT_B) \tag{3.28}$$

where the number of batches n_B can be obtained by

$$\left\lfloor \frac{T_{obs}}{T_B} \right\rfloor \tag{3.29}$$

The signal belonged to each block is defined as

$$x_i(t) = x_{ref}(t + iT_B)\, q(t) \tag{3.30}$$

where $x_{ref}(t)$ is the transmitted signal of opportunity and $q(t)$ is defined as

$$q(t) = \begin{cases} 1 & t \in [0, T_B] \\ 0 & otherwise \end{cases} \tag{3.31}$$

Substituting eq. (3.28) into eq. (3.27), the CAF can be written as

$$\chi(\tau, f_d) = \sum_{i=0}^{n_B-1} \int_0^{T_{\text{int}}} x_{surv}(t) x_i^*(t-\tau-iT_B) e^{-j2\pi f_d t} dt \tag{3.32}$$

Starting from the following equation

$$x_i^*(t-\tau-iT_B) \neq 0 \quad \forall t \in \left[iT_B+\tau, iT_B+\tau+T_B\right] \tag{3.33}$$

we can modify the integral in eq. (3.32) as

$$\chi(\tau, f_d) = \sum_{i=0}^{n_B-1} \int_{iT_B+\tau}^{iT_B+\tau+T_B} x_{surv}(t) x_i^*(t-\tau-iT_B) e^{-j2\pi f_d t} dt \tag{3.34}$$

Then, with a change of variable $\alpha = t - iT_B$, it now follows that eq. (3.34) yields:

$$\chi(\tau, f_d) = \sum_{i=0}^{n_B-1} e^{-j2\pi f_d iT_B} \int_{\tau}^{\tau+T_B} x_{surv}(\alpha+iT_B) x_i^*(\alpha-\tau) e^{-j2\pi f_d \alpha} d\alpha \tag{3.35}$$

Because τ is in the range *0* to $\tau_{\max}$, the limits of integration, expressed in eq.(3.35), become 0 and $T_B + \tau_{\max}$. In addition, eq. (3.34) can be reformulated as

$$\chi(\tau, f_d) = \sum_{i=0}^{n_B-1} e^{-j2\pi f_d iT_B} \int_{0}^{T_B+\tau_{\max}} x_i^{surv}(\alpha) x_i^*(\alpha-\tau) e^{-j2\pi f_d \alpha} d\alpha \tag{3.36}$$

where $x_i^{surv}(t)$ is the i-th block of the surveillance channel, $x_{surv}(t)$, and it is defined as

$$x_i^{surv}(t) = x_{surv}(t+iT_B)\, g(t) \tag{3.37}$$

where $g(t)$ is

$$g(t) = \begin{cases} 1 & t \in \left[0, T_B+\tau_{\max}\right] \\ 0 & otherwise \end{cases} \tag{3.38}$$

As it is possible to note from eq. (3.37) and Figure 3.4, the blocks on the surveillance channel are partially overlapped. By considering $x_i^{surv}(t)$ and $x_i(t)$, the CAF can be defined as

$$\psi_i(\tau, f_d) = \int_{-\infty}^{+\infty} x_i^{surv}(t) x_i^*(t-\tau) e^{-i2\pi f_d t} dt \tag{3.39}$$

Thus, substituting eq. (3.39) into eq. (3.36) we obtain

$$\chi(\tau, f_d) = \sum_{i=0}^{n_B-1} e^{-j2\pi f_d i T_B} \psi_i(\tau, f_d) \tag{3.40}$$

where $0 \le \tau \le \tau_{\max}$ and $-f_{d\max} \le f_d \le f_{d\max}$

The cross ambiguity function between $x_{surv}(t)$ and $x_{ref}(t)$ can be seen as a weighed sum of the ambiguity functions calculated within each batch.

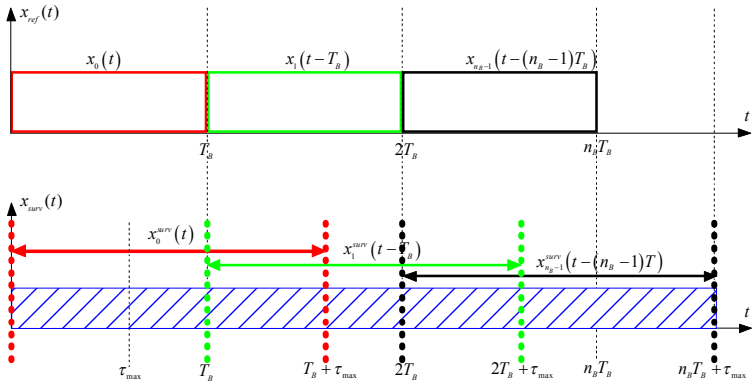

Figure 3.4 Reference and surveillance signals segmentation

In eq. (3.36), when the product between T_B and the maximum target Doppler $f_{d\max}$ is small compared to unity, we can approximate the phase rotation within each block as a constant

$$e^{-j2\pi f_d \alpha} \approx e^{-j2\pi f_d T_B} \quad \forall f_d \in \left[-f_{d\max}, f_{d\max}\right] \tag{3.41}$$

and eq. (3.36) can be simplified as

$$\chi_b(\tau, f_d) = e^{-j2\pi f_d T_B} \sum_{i=0}^{n_B-1} e^{-j2\pi f_d i T_B} \int_0^{T_B+\tau_{\max}} x_i^{surv}(\alpha) x_i^*(\alpha-\tau) d\alpha \tag{3.42}$$

where the subscript "b" stands for "batches algorithm".

Defining the cross correlation within the i-th block as

$$x_{cc}^i(\tau) = \int_0^{T_B+\tau_{\max}} x_i^{surv}(\alpha) x_i^*(\alpha-\tau) d\alpha \tag{3.43}$$

we may write the eq. (3.36) as

$$\chi_b(\tau, f_d) = e^{-j2\pi f_d T_B} \sum_{i=0}^{n_B-1} e^{-j2\pi f_d i T_B} x_{cc}^i(\tau) \tag{3.44}$$

The Doppler frequency compensation is neglected inside each block while it is considered with respect to consecutive blocks.

The main steps of this approach, schematically shown in Figure 3.5, can be summarized as:

- Select n_B consecutive batches of the reference channel $x_i(t)$ (see eq.(3.30)) , and the surveillance channel $x_i^{surv}(t)$ (see eq. (3.37))
- Iteratively, for $i = 0,...n_B - 1$:
  - Calculate the cross correlation, defined as $x_{cc}^i(\tau)$, between $x_i(t)$ and $x_i^{surv}(t)$ (see eq. (3.43))
- The Doppler dimension is then obtained by performing a FFT over the cross correlation values for each time delay, τ , or range bin

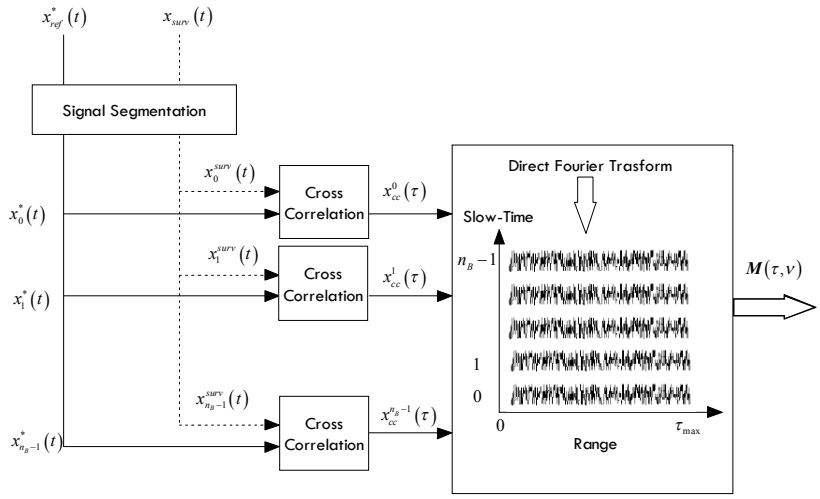

Figure 3.5 Reference and surveillance signals segmentation

3.2. MULTIPLE DVB-T CHANNEL

All blocks of the processing chain presented in this chapter are able to process single and multiple DVB-T signal. Only in the DVB-T signal reconstruction block is necessary to acquire the reference signal via wideband receiver, then each DVB-T channel is extracted and decoded, finally the three channels are recombined as shown in Figure 3.6.

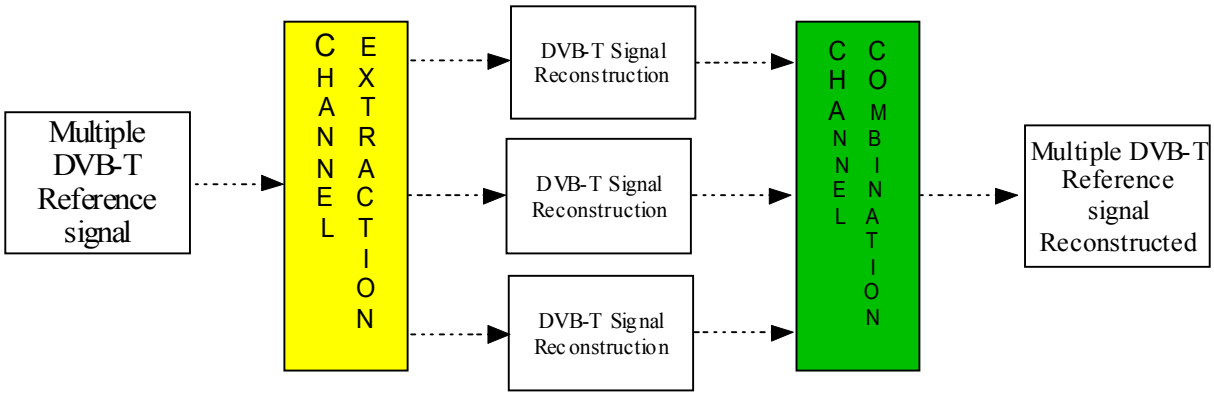

Figure 3.6 Multiple DVB-T channel combination scheme

Chapter 4.

PROCESSING RESULTS

4.1. DVB-T PRE-PROCESSING

Purpose of the reference signal pre-processing block is to filter the reference signal in order to remove noise, multipath and spikes in range Doppler maps due DVBT periodic reference signal and pilot tones (see par. 3.1.1).

The reference signal pre-processing in composed by two blocks:

1. The DVBT signal reconstruction, which purpose is to remove multipath from the reference signal (see par. 3.1.1.1)
2. The DVBT signal equalization, which purpose is to remove periodic reference signals and pilot tones attenuating spikes in range Doppler maps (see par. 3.1.1.2)

The reference signal pre-processing takes as input the reference signal from the yagi antenna and provides the input to the zero Doppler and cross-correlation algorithm.

Since the zero Doppler filter needs as input a signal as similar as possible to the original transmitted DVBT signal, it takes as input the output of the DVBT signal reconstruction module The output of the DVBT signal equalization can be provided to the cross correlation function ensuring a reduction of spikes in the range Doppler map.

For this test a multichannel DVB-T real data been considered.

Figure 4.1 shows the 64-QAM constellations before and after the signal reconstruction for three channels. It is clear that after the reconstruction a lot of noise has been removed, thus allowing better performance of the zero Doppler filter and consequentially of the whole radar processing chain.

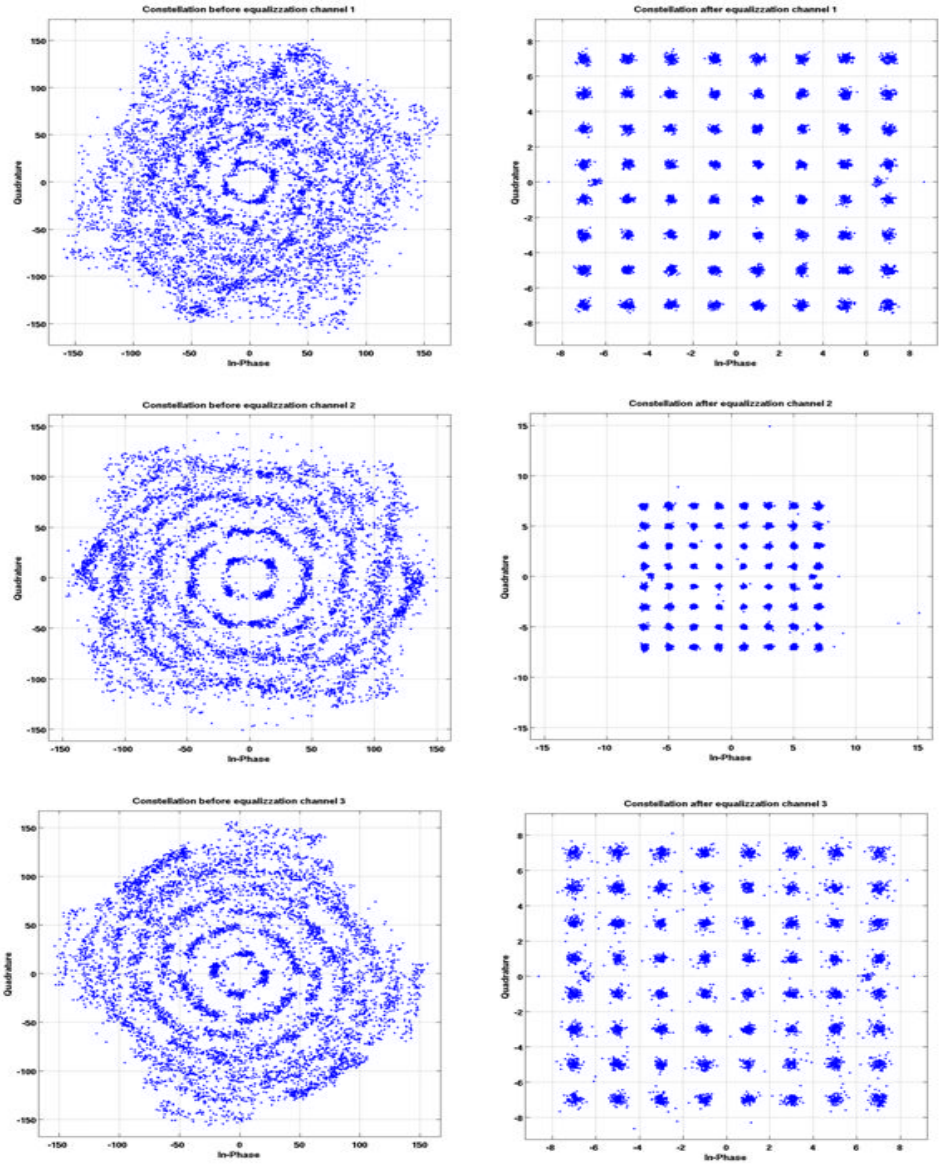

Figure 4.1 Reference signal constellation before and after reconstruction for every channel

In order to show the effectives of the signal reconstruction in range Doppler maps, Figure 4.2, Figure 4.3 and Figure 4.4 show the following autocorrelation functions:

- blue line: autocorrelation function of non-reconstructed reference signal. It is possible to see two peaks around $-17\mu s$ and $17\mu s$ due to some multipath.
- green line: correlation between the non-reconstructed reference signal and the reconstructed reference signal. The multipath peak is visible only in the positive delay around $17\mu s$.

- red line: autocorrelation of the reconstructed reference signal. Multipath peak disappears for both positive and negative delays at $-17\mu s$ and $17\mu s$)

This figure is useful to understand the effectiveness of the decoding operation, because it allows to eliminate the multipath on the reference signal.

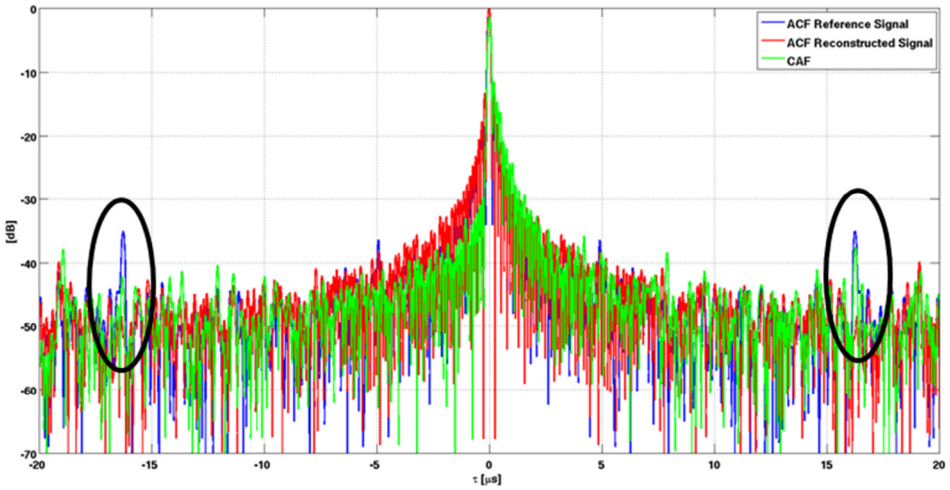

Figure 4.2 Effectiveness of the signal reconstruction (range profile). Circles show multipath peaks

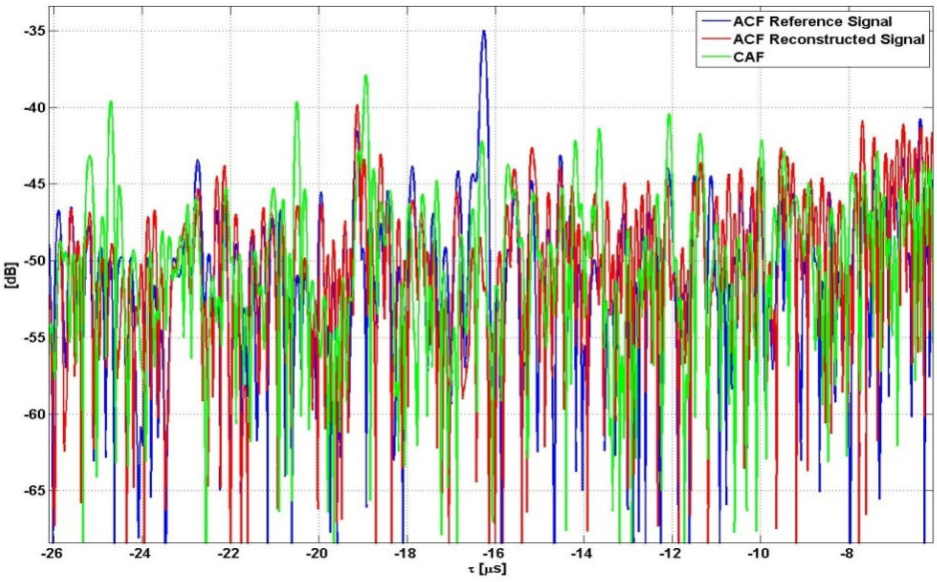

Figure 4.3 Effectiveness of the signal reconstruction (range profile). Zoom for negative delays

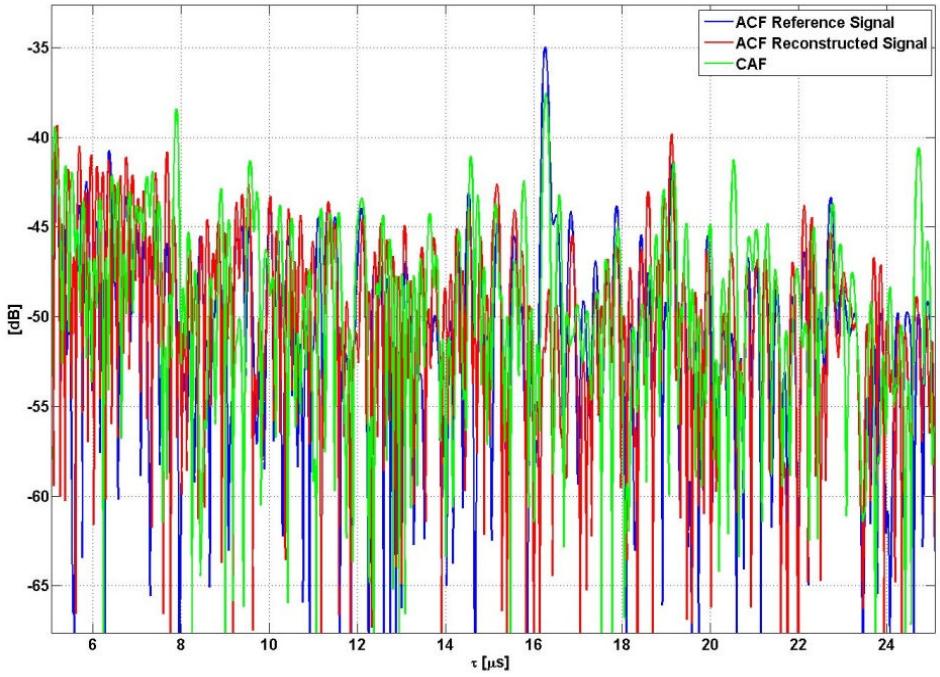

Figure 4.4 Effectiveness of the signal reconstruction (range profile). Zoom for positive delays

Figure 4.5 and Figure 4.6 show the cross correlation of the reference signal before and after the signal equalization. It can be seen that after the signal equalization the peaks due to periodic references in the DVBT signal have been strongly attenuated.

Table 4.1 provides numerical evaluations of the obtained attenuations.

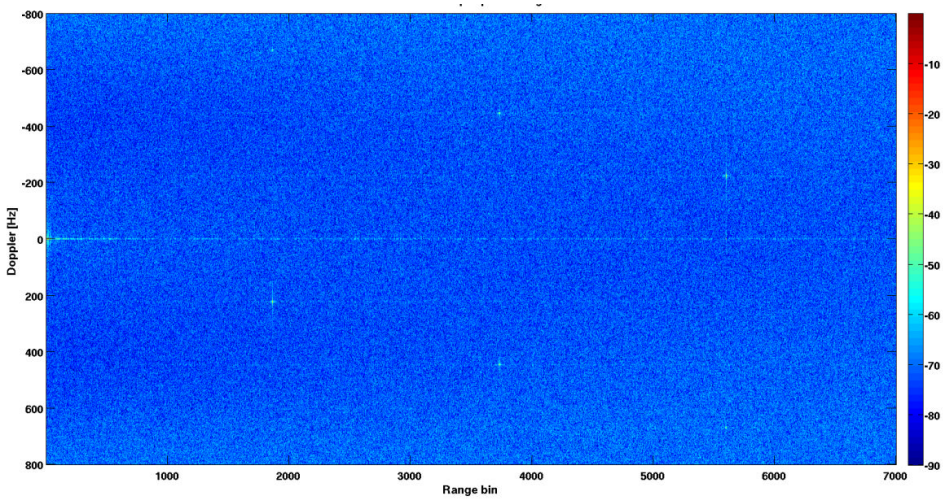

Figure 4.5 Reference signal Ambiguity Function before equalization

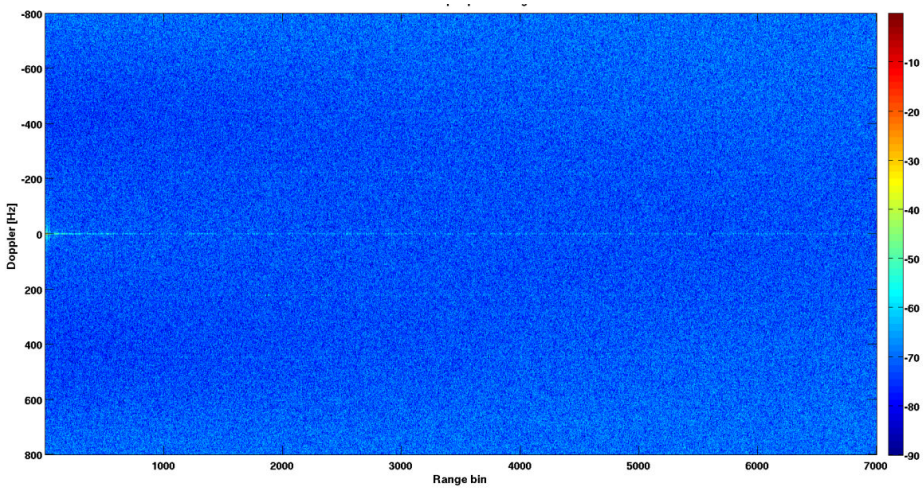

Figure 4.6 Cross Ambiguity Function between reference signal after equalizing and reference signal

Peak	*Range Bin*	*Doppler (Hz)*	*Peak Value (dBs)*	*Peak filtered (dBs)*	*Peak reduction (dBs)*
1	1867	-669	-51.15	-85.89	34.7
2	1867	223	-30.81	-97.93	67.12
3	3734	-446	-31.19	-100.4	69.21
4	3734	446	-33.55	-89.95	56.4
5	5601	-223	-28.82	-78.4	49.6
6	5601	669	-35.44	-84.23	48.79

Table 4.1 Numerical Evaluations of the attenuations

4.2. ZERO DOPPLER INTERFERENCES SUPPRESSION

To evaluate the performance of the considered technique, we select a specific case. We consider a single DVB-T signal received by Yagi antenna (Observation time=0.5s and $f_s = 9.14MHz$). The scenario consists of direct signal with a Direct signal to Noise Ratio (DNR) of about 60dB, with multipath and Clutter to Noise Ratio (CNR) of about 50 dB and five target echoes whose characteristics are listed in Table 4.15.

Target	***Range Bin***	***Doppler (Hz)***	***DNR (dB)***	***CNR (dB)***	***SNR (dB)***	***SINR (dB)***
1	30	-10	60	50	8.9	17
2	300	100	60	50	3.2	8.46
3	400	15	60	50	1.1	8.42
4	500	-30	60	50	-4.5	3.16
5	600	80	60	50	-8	2.15

Table 4.2 Target echoes parameters for the reference scenario

To evaluate the disturbance cancellation capability of adaptive algorithms, the Signal Interference plus Noise Ratio SINR can be defined as follows:

$$SINR_{dB} = 10\log_{10}\left(\frac{P_{\text{Target}}}{P_{\text{Clutter}}}\right) \tag{4.1}$$

Where P_{Target} is the power of returns of clutter where the target is located (blue square) and P_{Clutter} is the power of the target (red square) as shown in Figure 4.7.

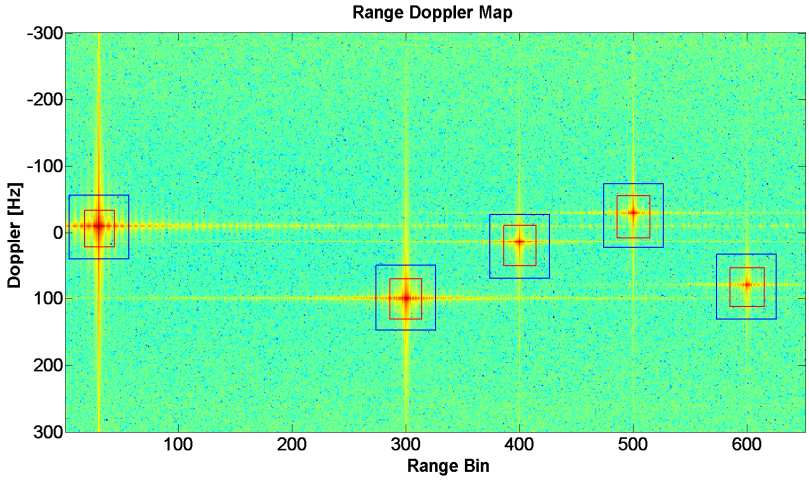

Figure 4.7 Target representation of the reference scenario

In the absence of cancellation a strong peak corresponding to direct signal, multipath and clutter are present at Range Doppler Map (Figure 4.47) while targets are completely masked by their side lobes.

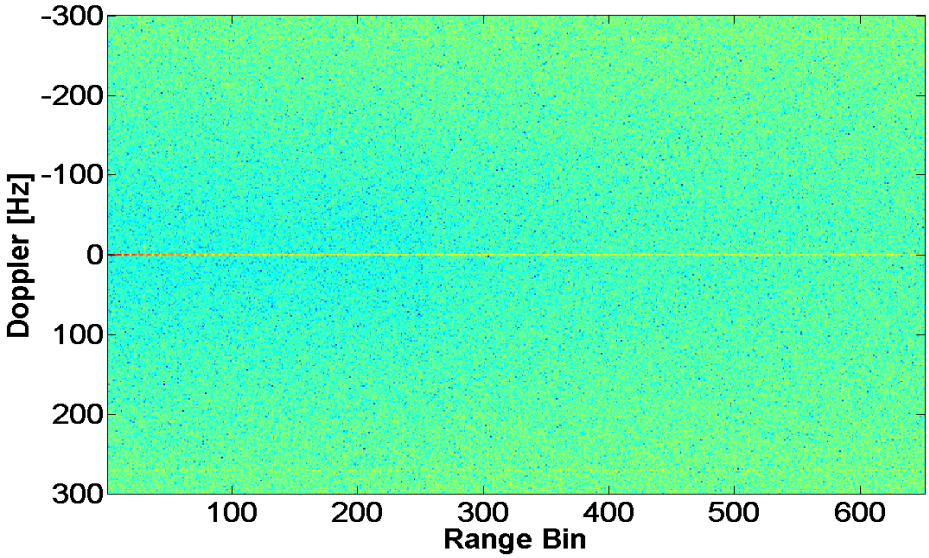

Figure 4.8 Range Doppler Map before direct signal and clutter cancellation

Figure 4.9 shows the Range Doppler Map evaluated at the output of the considered algorithm with a weight vector dimension $M = 8$.

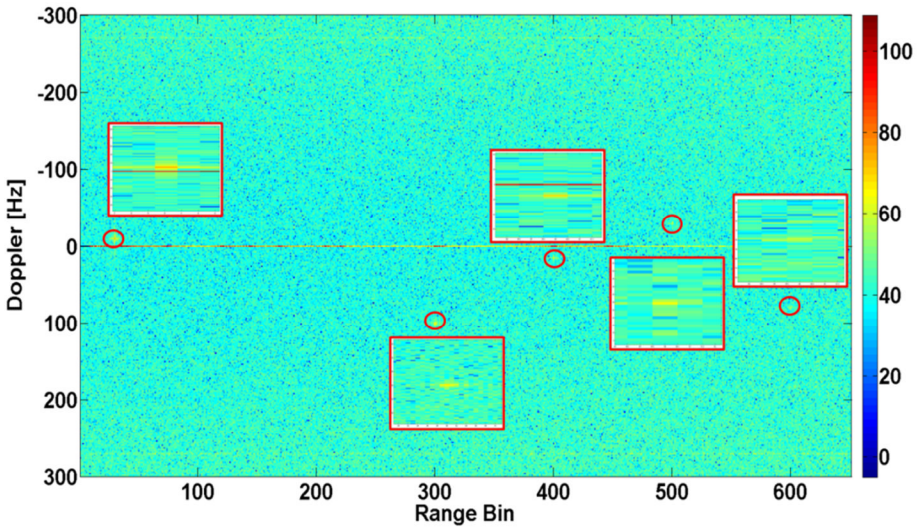

Figure 4.9 Range Doppler Map after LS filtering

The following considerations are a result of an extensive performance analysis which has been performed for the reference scenario as previously described.
To classify this method in terms of performances, we identified some parameters like:

- Elapsed Time or elaboration time
- SINR (describe in the previous section)

The LS algorithm have been applied to different weight vector dimensions and have been compared with Normalized Least Mean Square (NLMS) [25][26] algorithm (Figure 4.10, Figure 4.11) in order to find the better compromise between computational load and cancellation capability.

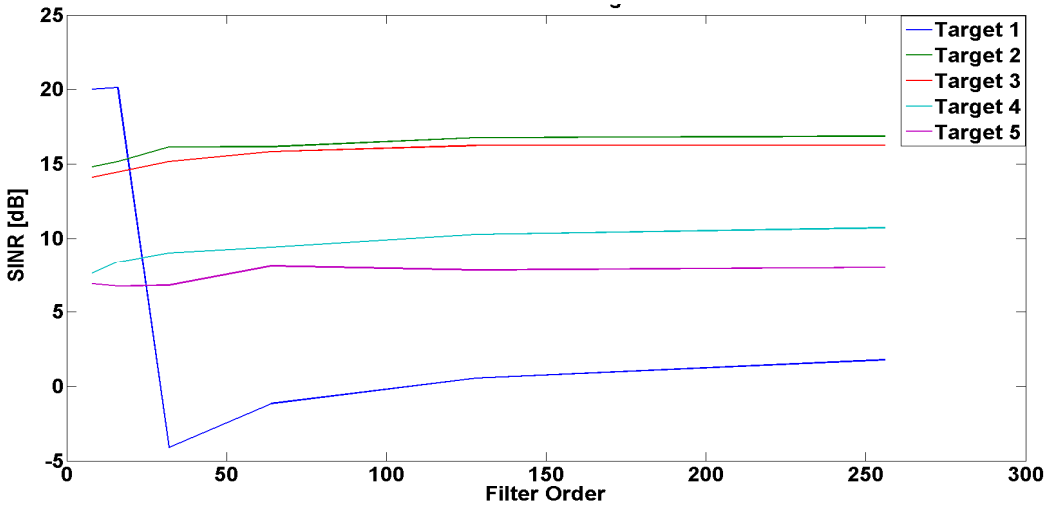

Figure 4.10 SINR values of each targets after NLMS filtering for different weight vector

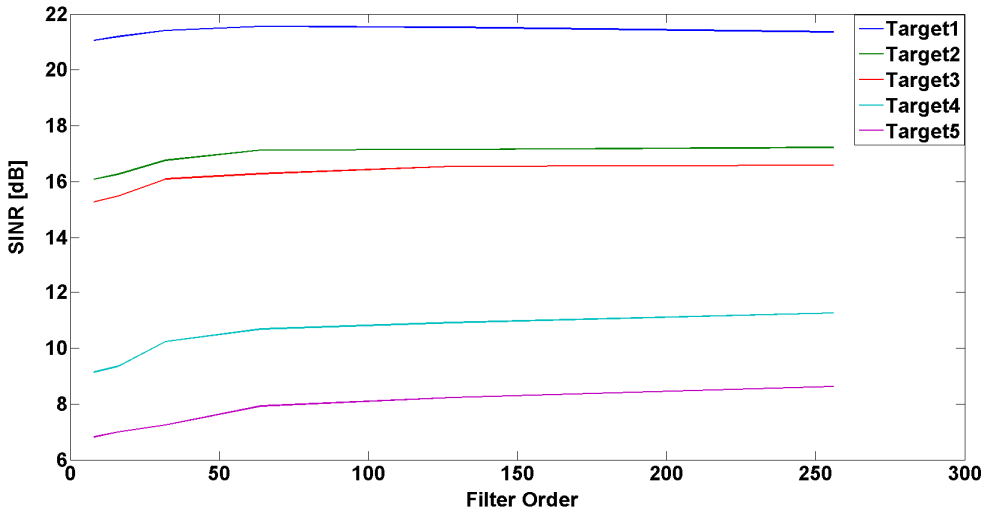

Figure 4.11 SINR values of each targets after LS filtering for different weight vector

The SINR values of Target 1 (blue line) after NLMS filtering show lower values with respect to LS. This effect yields a partial cancellation of target echo whose delay is included in the cancelled area.

It can be noted that the SINR values of each target do not increase linearly when the filter order increases.

Moreover Figure 4.12 shows the time processing comparison among LS and NMLS filters. It is worth noting that LS filtering is faster than NLMS filtering for small weight vector dimensions.

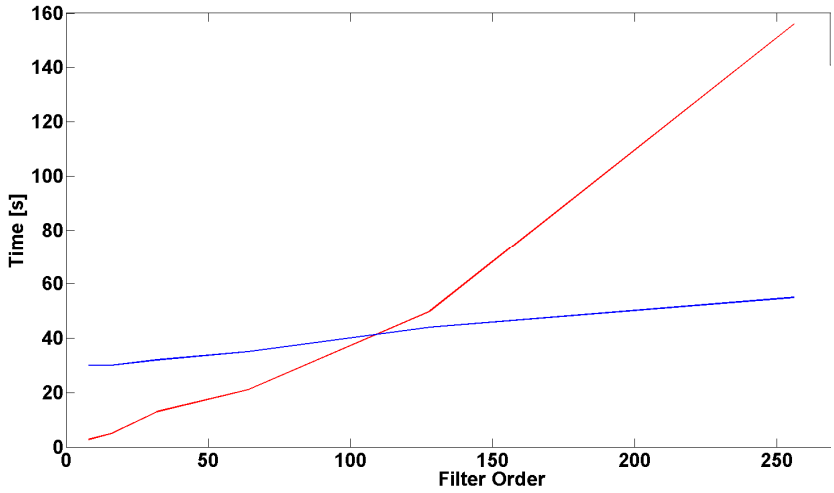

Figure 4.12 Time processing elapsed for LS (red line) and NLMS (blue line) filtering

The performed analysis has shown that LS algorithm allows an almost complete clutter cancellation and it is faster than other algorithms for small vector dimensions.

Therefore the LS filter with a weight vector dimension of 100 represents the better compromise between computational load and cancellation capability in our reference scenario. An improvement of about 5-10 dB of SINR is obtained as reported in the Table 4.3.

Target	***Range Bin***	***Doppler (Hz)***	***DNR (dB)***	***CNR (dB)***	***SINR input (dB)***	***SINR output (dB)***
1	30	-10	60	50	17	22
2	300	100	60	50	8.46	17
3	400	15	60	50	8.42	16
4	500	-30	60	50	3.16	11
5	600	80	60	50	2.15	8

Table 4.3 SINR values after LS filter (last column)

4.3. 2-D MATCHED FILTER

In this section, we discuss the results that have been obtained by considering a 8K DVB-T transmitted signal [24]. The surveillance channel signal has been modelled as

$$x_{surv}(t) = x_{ref}(t-\tau_T)e^{i2\pi f_{d_T}t} + w(t) \tag{4.2}$$

where τ_T, f_{d_T} are the actual time delay and Doppler shift of a single slowly fluctuating point target and $w(t)$ is a Gaussian white noise process. Typically, the radar performances are evaluated in terms of signal to noise ratio (SNR). However, the noise power at the output of the optimum and batch algorithm is the same. Therefore, to evaluate the losses of the batches algorithm with respect to the optimum algorithm, we define the following parameter

$$Loss(\tau_T, f_{d_T}) = 20\log_{10}\left(\left|\frac{\chi_b(\tau_T, f_{d_T})}{\chi(\tau_T, f_{d_T})}\right|\right) \tag{4.3}$$

where $\chi(\tau_T, f_{d_T})$ is the target peak calculated with optimum method and $\chi_b(\tau_T, f_{d_T})$ is the target peak calculated with the sub-optimum method. Equation (4.3) can be evaluated by using eq. (3.36) and eq. (3.42) as

$$\begin{aligned} Loss(\tau_T, f_{d_T}) &= 20*\log_{10}\left(\left|\sum_{i=0}^{n_B-1}\psi_i\left(0,-f_{d_T}\right)/\sum_{i=0}^{n_B-1}\psi_i(0,0)\right|\right)\approx \\ &\approx 20*\log_{10}\left(\left|\frac{n_B\overline{\psi}_i\left(0,-f_{d_T}\right)}{E_i}\right|\right) \end{aligned} \tag{4.4}$$

We can observe that the losses depend only on the target Doppler frequency and on the shape of the ambiguity function. A detailed analysis has been conducted by evaluating the losses with respect to the Direct-FFT method [27]. The simulations were useful to find a length of the batch that is able to give a good compromise between losses and processing time. A total of 48 different range Doppler target positions have been considered. For each range Doppler position, 100 realizations have been done. The analysed CAF algorithm has been applied for five different batch lengths. The parameters used during the simulations can be summarized as:

- Sampling Frequency $f_s = 9.14MHz$

- $T_{obs} = 250ms$
- $f_{d_{MAX}} = 1500Hz$
- Target Doppler frequency: $f_{d_T} = [0, 100, 200, 300, 400, 500, 600, 700] Hz$
- Target time delay: $\tau_T = [5.46, 16.40, 27.34, 38.28, 49.22, 60.16] \mu s$
- Batch time: $T_B = [15.64, 31.28, 109.38, 218.76, 333.29] \mu s$

Figure 4.13 shows the processing time for different range bins averaged on 800 realizations. The simulation time has been evaluated with a general purpose 4 core PC equipped with 8 GB of RAM. As it is possible to note, the processing time is strongly reduced (more than 96%) with respect to the Direct FFT method.

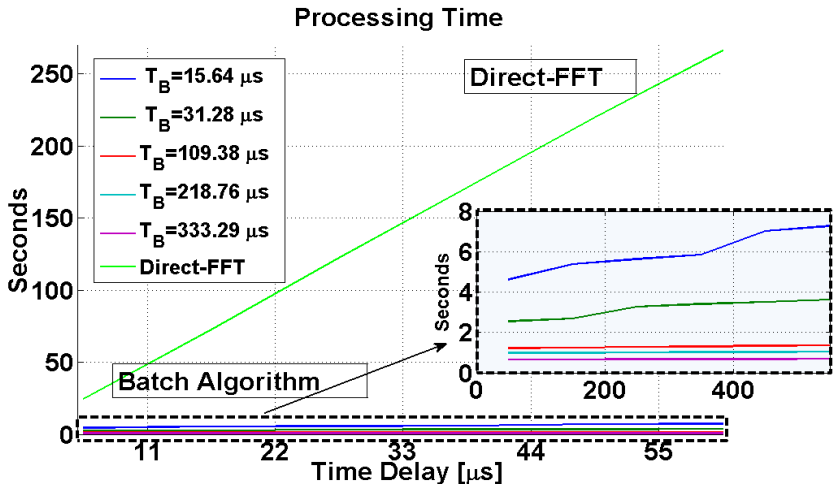

Figure 4.13 Time processing elapsed for Direct FFT method and batch algorithm

Moreover the ratio between the target power calculated with both the Direct-FFT method and the Batch method has been shown in Figure 4.14 and Figure 4.15. The losses of the target power are negligible along the range (Figure 4.14). On the contrary, as long as the target Doppler frequency and the batch length increase, the target power decreases (Figure 4.15).

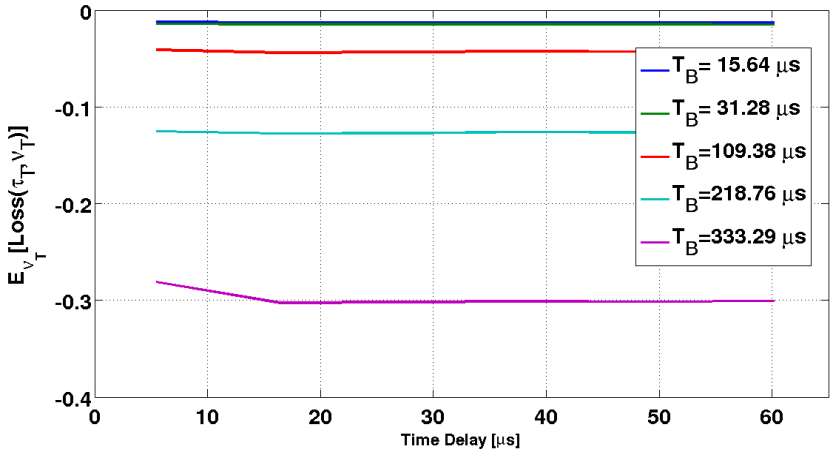

Figure 4.14 Losses of the target power averaged with respect to the Doppler frequencies

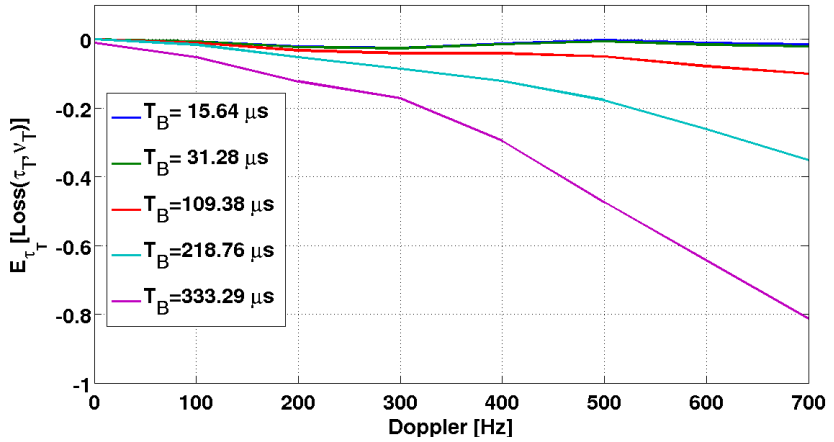

Figure 4.15 Losses of the target power averaged with respect to the range bin

Simulation results have proven that the proposed algorithm is able to perform comparably with the complete calculation of the CAF whilst strongly reducing the computational effort.

Chapter 5.

PASSIVE BISTATIC RADAR DEMONSTRATOR DESCRIPTION

5.1. SOFTWARE DEFINED RADIO

A number of definitions can be found to describe Software Defined Radio, also known as Software Radio or SDR. Simply Software Defined Radio is defined as [28] :

"Radio in which some or all of the physical layer functions are software defined"

Traditional hardware based radio devices limit cross-functionality and can only be modified through physical intervention. This results in higher production costs and minimal flexibility in supporting multiple waveform standards. By contrast, software defined radio technology provides an efficient and comparatively inexpensive solution to this problem, allowing multimode, multi-band and/or multi-functional wireless devices that can be enhanced using software upgrades.

In Table 5.1 a list of some software-defined radio boards/subsystem providers is reported.

Providers	Site
DataSoft Corporation	http://www.datasoft.com/
Ettus Research	http://www.ettus.com/
Innovative Integration	http://www.innovative-dsp.com/
Pentek	http://www.pentek.com/
Spectrum Signal Processing by Vecima	http://www.spectrumsignal.com/

Table 5.1 SDR boards/subsystem providers

5.2. ETTUS BOARD

Unlike other off-the-shelf options, the USRP family Ettus Board [29] represents a complete and versatile solution. The needs for the experiments included a board able to acquire different types of waveforms, and therefore a flexible on the RF frontend. The hardware is able to easily change carrier frequency, RF gain, channel bandwidth, etc. The demonstrator also required an ability to receive from two synchronized channels simultaneously. All of these capabilities were provided by the USRP2 hardware (Figure 5.2 and Figure 5.2).

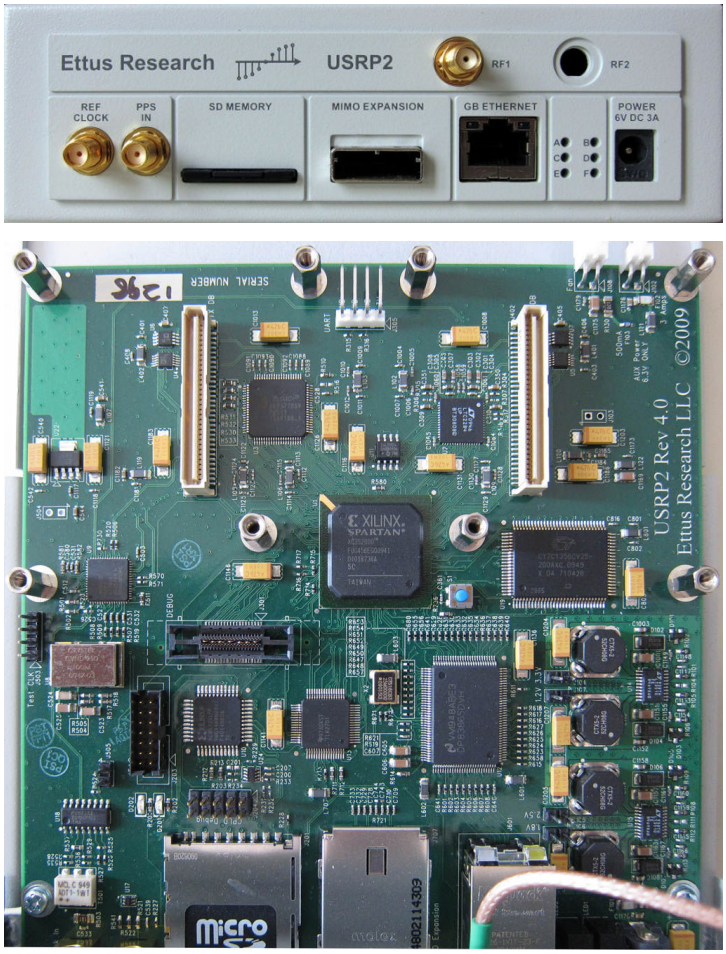

Figure 5.1 USRP2 Board

Figure 5.2 MIMO cable used to link a pair of USRP2 systems together

The main technical specifications of the USRP2 are:

- FPGA Xilinx Spartan 3-2000 EP1C12 Q240C8 “Cyclone”
- 2 High-Speed Analog to Digital Converters (ADCs) operating at 14 bits with a sampling rate of 100 Mega-samples per seconds (100 MS/s)
- 2 High-Speed Digital to Analog Converters (DACs) operating at 16 bit with a sampling rate of 400 MS/s
- Gigabit Ethernet interface

The USRP2 is able to acquire I/Q signals up to 25 MHz of bandwidth.

The primary driver for all Ettus Research products, including the USRP2, is UHD, the Universal Hardware Driver. UHD is considered stable and actively maintained by Ettus Research. It’s open source, but it can be linked to without requiring the linking software be open source. It's possible to use UHD with GNU Radio.

The aim of GNU Radio is to develop SDR terminals. In particular, this project provides a collection of software modules to perform the main operations for signal processing. It is interesting to note that the GNU Radio paradigm currently gathers a very active worldwide community of developers building their projects upon this platform. The GNU Radio framework is split in two wide areas. the first one makes use of the C++ programming language, while the latter one exploits the flexibility provided by the python scripting language.

5.3. RF FRONT-END

The daughterboards are basic RF front-ends specifically designed to expand the USRP's capabilities. They include various functions depending on the frequency band to be accessed and connection points for antennas. Table 5.2 lists the daughterboards currently available from Ettus Research. The Basic boards have no tuning or amplification, and are essentially interfaces to the USRP for external front ends. All other boards have tuning and amplification.

Model	Type	Freq	Bandwidth(MHz)**	Power Output(mW)	Noise Figure(dB)
TVRX2	Rx	50 MHz - 860 MHz	10	n/a	4-10
RFX900	Tx/Rx, Full-Duplex	750 MHz - 1050 MHz	30	200	5-10
RFX1200	Tx/Rx, Full-Duplex	1150 MHz - 1450 MHz	30	200	5-10
RFX1800	Tx/Rx, Full-Duplex	1.5 GHz - 2.1 GHz	30	100	5-10
RFX2400	Tx/Rx, Full-Duplex	2.3 GHz - 2.9 GHz	30	50	5-10
WBX	Tx/Rx, Full-Duplex	50 MHz - 2.2 GHz	40	100	5-10
SBX	Tx/Rx, Full-Duplex	400 MHz - 4.4 GHz	40	100	5-10
XCVR2450	Tx/Rx, Half-Duplex	2.4 GHz - 2.5 GHz	33	100	5-10
DBSRX2	Rx	800 MHz - 2.35 GHz	1 - 60 MHz	N/A	4-8
LFTX	2 x Tx	DC - 30 MHz	60*	1	N/A
LFRX	2 x Rx	DC - 30 MHz	60*	N/A	N/A
BasicTX	2 x Tx	1 MHz - 250 MHz	100*	1	N/A
BasicRX	2 x Rx	1 MHz - 250 MHz	100*	N/A	N/A

Table 5.2 Ettus daughterboards

The RF Front-end used for the passive bi-static radar experiments is composed by the DBSRX daughterboard (Figure 5.2). The key feature of this configuration is the ability to be tuned via software at 800 MHz or 2.1 GHz in order to exploit the two different IOs (DVB-T and UMTS [10]). During the preliminary tests we observed that the DBSRX is able to work also at frequencies up to 600MHz.

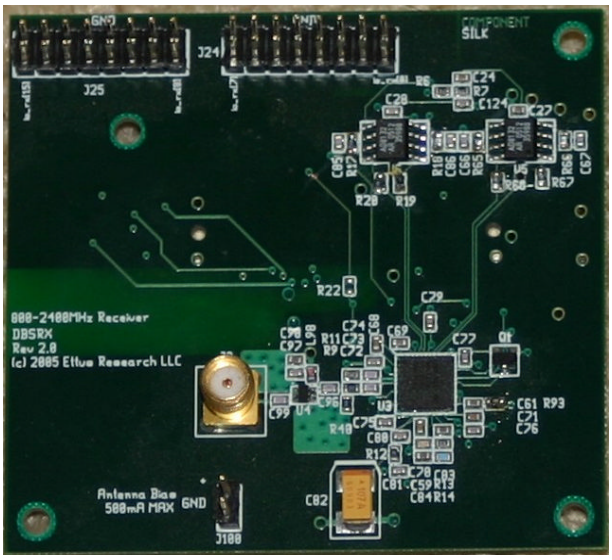

Figure 5.3 DBSRX daughterboard

The DBSRX features a software controllable channel filter which can be made as narrow as 1 MHz, or as wide as 60 MHz.

5.4. ANTENNA

The antenna used during preliminary measurements and the experiment for the surveillance channel is a Yagi-Uda antenna with 95 elements and 2m length with a receiving gain equal to 18 dB and a Half Power Beam Width of 20 degrees in the horizontal plane.

The irradiation pattern for surveillance antenna is presented in Figure 5.4

On the reference channel, a Yagi-Uda antenna with 47 elements and a gain of 15 dB has been chosen to point the illuminator of opportunity.

The irradiation pattern for reference antenna is presented in Figure 5.5.

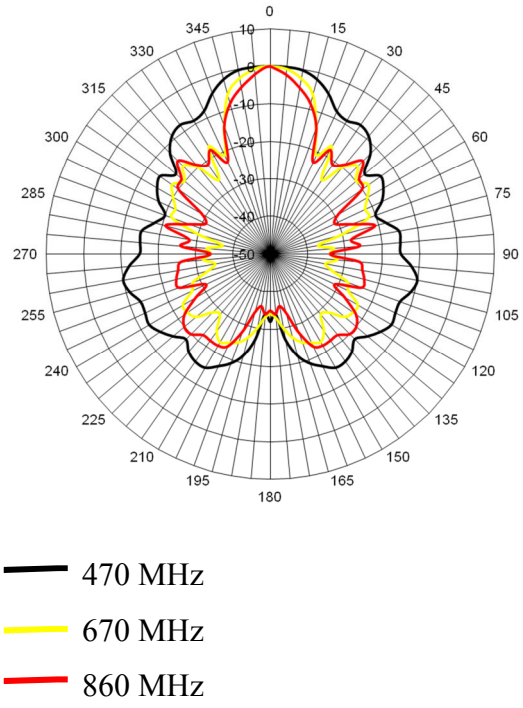

a) **b)**

Figure 5.4 a) Surveillance Antenna b) Radiation Pattern for 95 elements antenna at different frequencies

a)

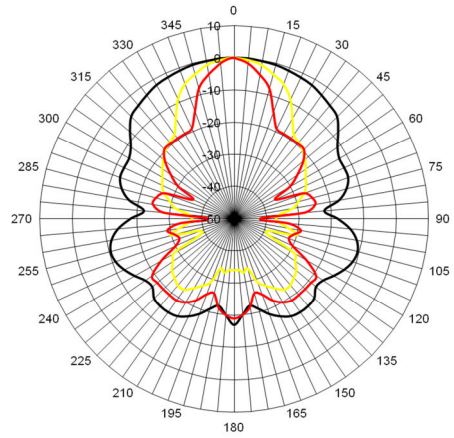

b)

Figure 5.5 a) Reference Antenna b) Radiation Pattern for 47 elements antenna at different frequencies

5.5. SIGNAL PROCESSING

A signal processing scheme of a passive radar demonstrator is sketched in Figure 5.6

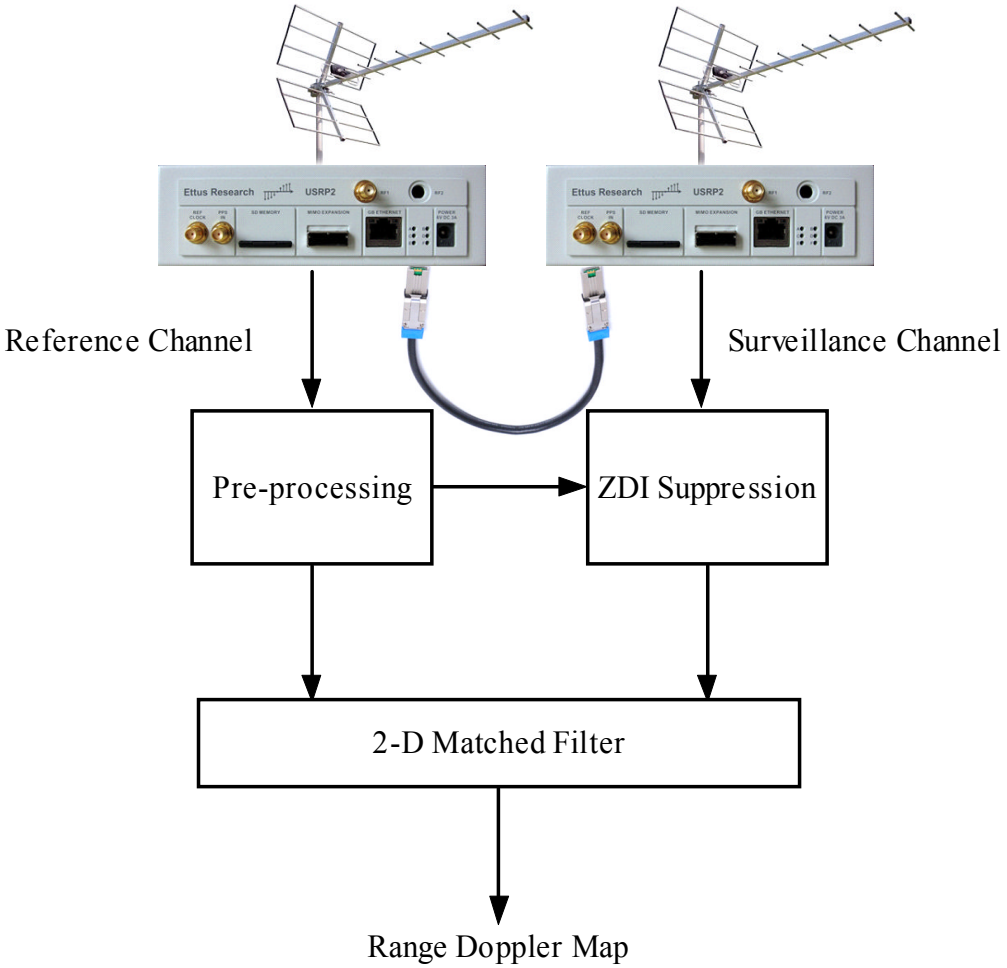

Figure 5.6 Signal Processing scheme

The system management and control was implemented in a C++ framework using the UHD API. The main functionalities relate to tuning, filtering, amplification, sampling, decimation and data transfer. Finally, all the radar signal processing algorithms, previously described (Chapter 3), have been implemented in MATLAB® and processed on a General-Purpose computer.

All equipment used during the experiments is summarized in Figure 5.7

Figure 5.7 DVB-T Passive Radar Demonstrator Equipment

Chapter 6.

HIGH RANGE RESOLUTION MULTICHANNEL DVB-T PASSIVE RADAR EXPERIMENTS

6.1. SCENARIOS DESCRIPTION

In the last part of this work, we carried out experiments regarding the feasibility of a passive radar with a low cost equipment by using a software defined architecture described in Chapter 5 and showed in Figure 6.1

Figure 6.1 DVB-T Passive Radar Demonstrator

Experiments have been conducted for two different scenarios aerial and maritime in order to demonstrate the feasibility and also the flexibility of the proposed solution.

The scenario of interest was defined before each experiment. Then, to highlight the improvements by using DVB-T multichannel signal, for each experiment, a comparison between single channel and multichannel detection has been done.

6.2. AERIAL SCENARIO EXPERIMENT

The experiment scenario geometry is shown in Figure 6.2. Specifically, the receiver was located at the Department of Information Engineering of the University of Pisa and the DVB-T transmitter was 14 km away from the receiver at a bearing of 36° North-East as indicated by the green line. The surveillance antenna was pointed at 17° with respect to North (i.e.: azimuth) and tilted upwards towards the sky at an angle of 30°. The central frequency of DVB-T signal is 754 MHz.

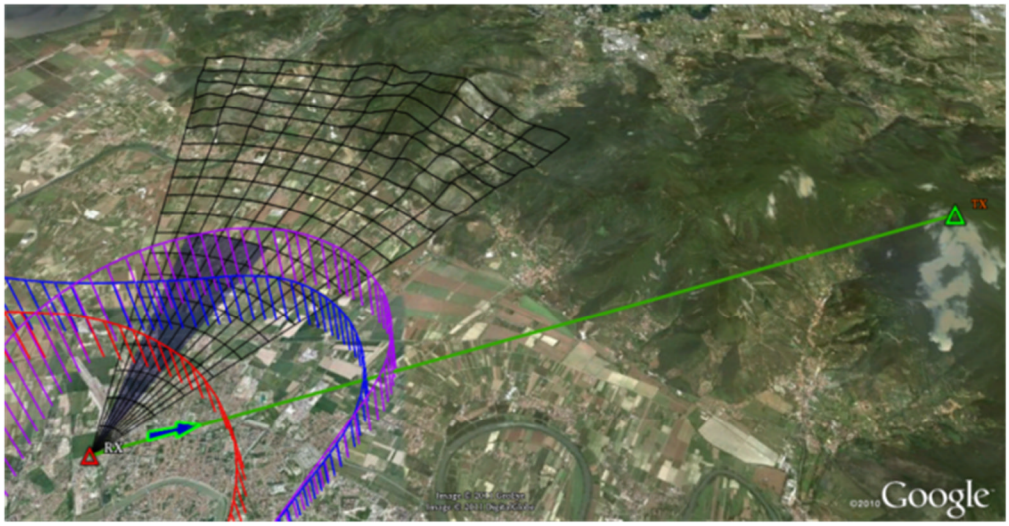

Figure 6.2 Experiment Scenario geometry and target trajectories (Aerial Scenario)

Figure 6.2 shows typical trajectories of targets taking off from the Pisa airport. During the experiments an ADS-B (Automatic Dependent Surveillance Broadcast) receiver was used. The ADS-B data contains information about geographical position, velocity, and heading of the targets and can be useful to check the detection results of the passive radar demonstrator. Particularly, starting from the ADS-B data, the Doppler frequencies of the targets of interest were calculated as a function of the azimuth position (shown in Figure 6.3). The black box highlights the expected Doppler frequencies when the targets were within the surveillance antenna main beam.

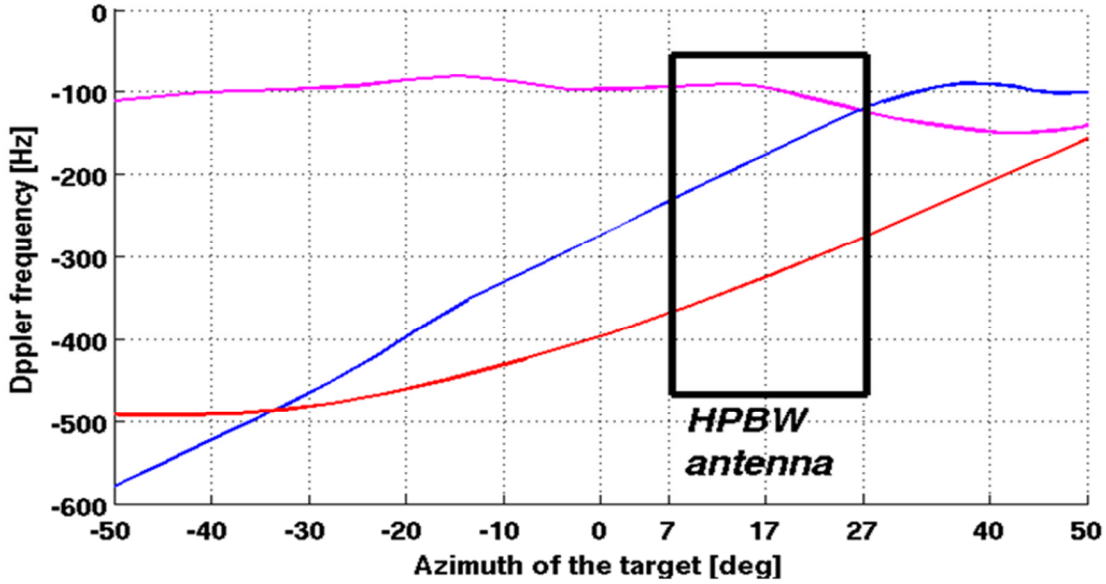

Figure 6.3 Doppler frequencies calculated exploiting the ADS-B data (velocity, heading and position of the target) as a function of the target azimuth position respect to the receiver

6.2.1. Results

The experiment scenario geometry is shown in Figure 6.2. The detected target is a British Airways Boeing 737-400 and the main physical specification can be summarized in

Length: 36 m

Wingspan: 28.9 m

Height: 11 m

Figure 6.4 Main technical information of the detected target

In a passive radar scenario the Doppler frequency is given by [30] :

$$f_d = \frac{1}{\lambda}\left[\frac{\vec{r}_1 \cdot \vec{v}}{|\vec{r}_1|} + \frac{\vec{r}_2 \cdot \vec{v}}{|\vec{r}_2|}\right] \tag{6.1}$$

Where $\vec{v}$ is the target velocity vector, $\vec{r}_1$ is the transmitter to target vector, $\vec{r}_2$ is the target-receiver vector. Within the distance of interest (1-3 km) and considering the Doppler frequency shown in Figure 6.3, the expected target velocity value ranges between 300 and 500 km/h.

After applying the pre-processing technique presented in the Chapter 3, the Cross-Ambiguity Function (CAF) relative to three adjacent DVB-T channels is calculated (Figure 6.5).

The peak due to the target echo is clearly visible at the 87th range bin (i.e.: about 1700 m for the geometry considered in Figure 6.2).

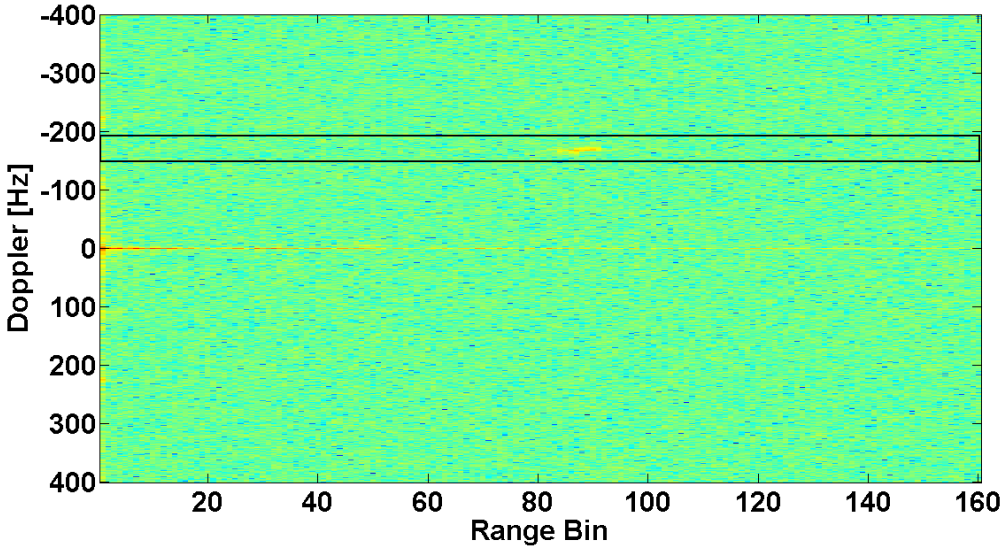

Figure 6.5 CAF of the surveillance area

In order to better evaluate the range resolution improvement, the CAF is calculated for both one and three DVB-T channels. Particularly, Figure 6.6 presents the range profile along the Doppler frequency of the target echo (i.e.: -169 Hz). Considering the geometry in Figure 6.2, the bistatic range resolution achievable by using a single channel is around 57 m, whereas, by exploiting three adjacent channels, it is around 18 m.

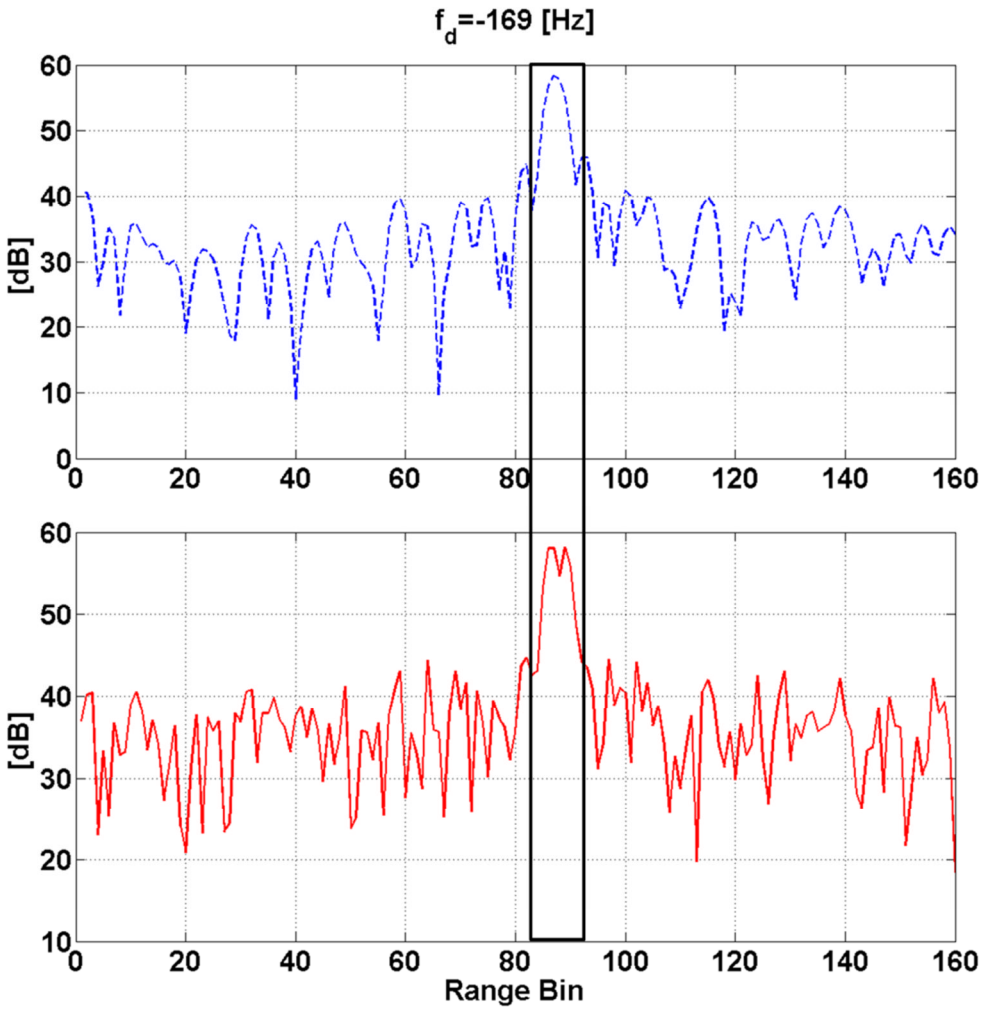

Figure 6.6 Target range profile for a single DVB-T channel (dashed line on the top) and for three adjacent DVB-T channels (solid line on the bottom)

Moreover, the target echo exhibits a Doppler frequency value of -169 Hz, which is in agreement with the expected velocity (more than 450 km/h).

The range resolution improvement obtained by exploiting three DVB-T channels (solid line) is evident when compared to the single DVB-T channel case (dashed line). In fact, the dashed line range profile shows only one main peak whereas two peaks are clearly visible on the solid line profile. The two main peaks relative to the target echo in the range profile are relative to different parts of the aircraft (Figure 6.6). Indeed this conclusion is in agreement with the target size and the achievable range resolution.

6.3. MARITIME SCENARIO EXPERIMENT

The experiment scenario geometry is shown in Fig. 2.

Figure 6.7 Experiment Scenario geometry and target trajectories (Maritime Scenario)

Specifically the receiver was located at the "CSSN-ITE G. Vallauri" institute in Livorno, the used illuminator of opportunity was a DVB-T transmitter located on "Monte Serra" in Pisa (around 32 km far from the receiver) and the surveillance antenna was directed towards an area of sea in front of the receiver site (Figure 6.8).

The used DVB-T channel carrier frequency is 754 MHz and the targets of interest were ships arriving and departing from the nearby harbour.

In Figure 6.9 the expected Doppler frequencies for ships departing from the nearby harbour are shown.

Within the distance of interest (1.5-3.3 nm) and in the assumption of ship speed ranging between 5 and 10 kts, the expected Doppler frequency absolute value will be comprised between 20 and 60 Hz.

Figure 6.8 Surveillance Area

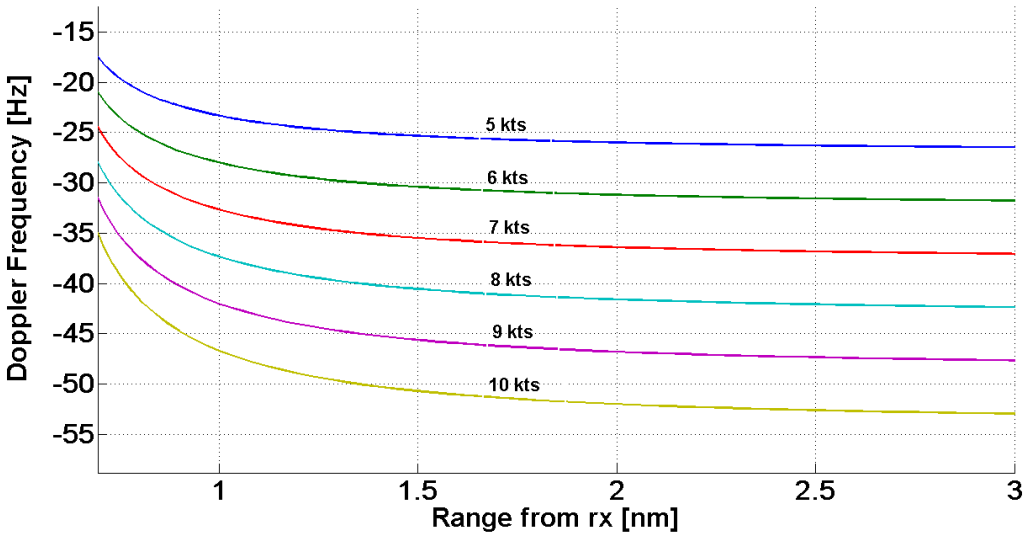

Figure 6.9 Expected Doppler frequencies for ships departing from the nearby harbor (receding from receiver)

6.3.1. Results

The surveillance area during the acquisition is shown Figure 6.10.

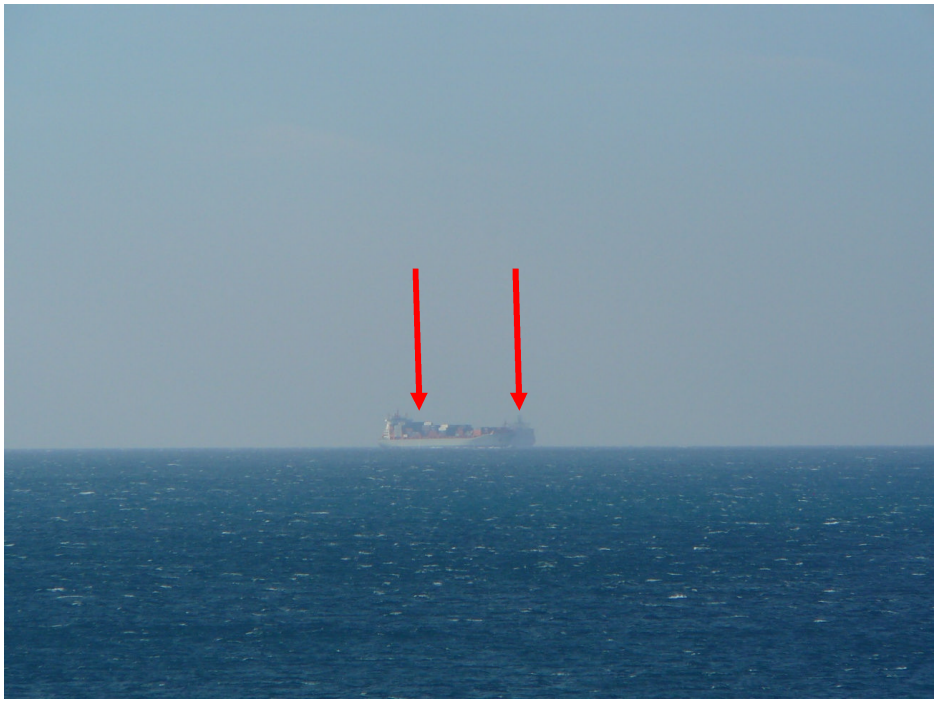

Figure 6.10 Surveillance area during the acquisition

On the reference channel a pre-processing technique and Zero Doppler Interference suppressor, presented in Chapter 3, have been used in order to reduce clutter echo and direct path interference. The Cross-Ambiguity Function (CAF) obtained after processing is presented in Figure 6.11.

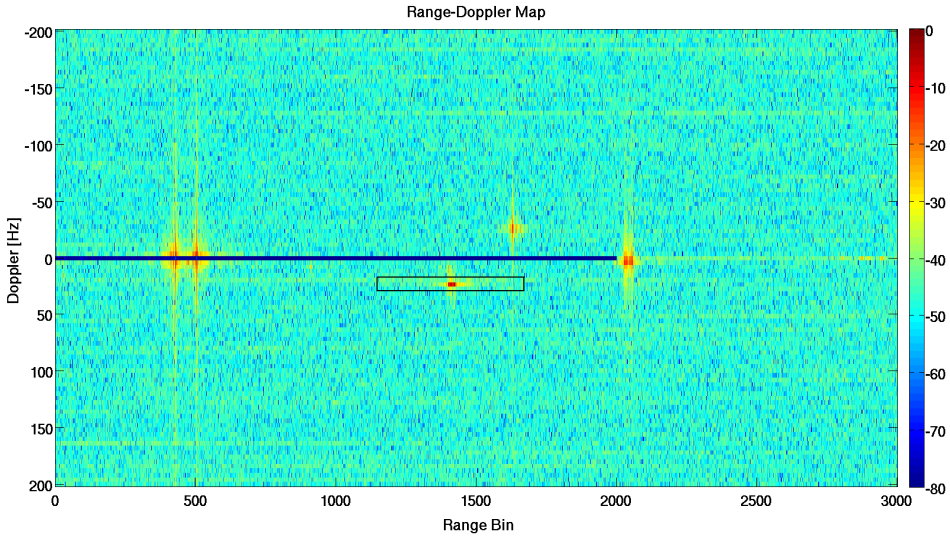

Figure 6.11 DVB-T CAF of the surveillance area

The echoes relative to the ships are clearly visible at a range bin 1450 and 1600 respectively. The Doppler frequencies are equal to -24 Hz and 30Hz (i.e.: about 5kts). It should be noted that the targets were cruising in opposite directions. In the Range Doppler are visible another target at range bin 2000 and a strong echo at zero Doppler frequency due to a stationary ship.

Also in this experiment in order to better evaluate the range resolution improvement, the CAF is calculated for both one and three DVB-T channels. Particularly, Figure 6.12 presents the range profile along the Doppler frequency of the target echo (i.e.: -25 Hz, black rectangle).

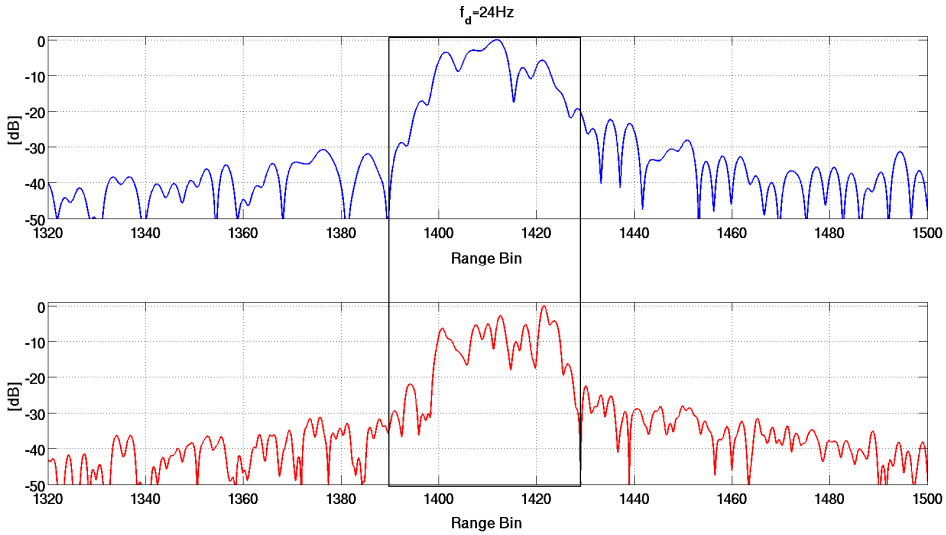

Figure 6.12 Target range profile for a single DVB-T channel (blue line on the top) and for three adjacent DVB-T channels (red line on the bottom)

The range resolution improvement obtained by exploiting three DVB-T channels (red line) is evident with respect to the single DVB-T channel case (blue line).

CONCLUSIONS

In this thesis the development of a DVB-T based full digital passive radar demonstrator has been investigated. The main features of the signal processing chain adopted in the passive radar demonstrator have been presented and analysed. A recent technology able to satisfy the requirements of reconfigurability and flexibility has been identified as the Software Defined Radio technology. Specifically this thesis focuses on the exploitation of a low cost SDR device called the USRP2 for radar applications.

The advantage of using multiple DVB-T channels for a passive radar system has been taken into account in order to enhance the radar range resolution. A preliminary study has been focused on the ambiguity function analysis in order to verify the suitability of a multichannel DVB-T signal for radar applications. The theoretical study has been supported by preliminary measurements relative to three adjacent DVB-T channels. Experimental results in aerial and maritime scenarios obtained with the Software Defined Passive Radar demonstrator developed in this thesis, have been carried out. The results showed a clear improvement in range resolution when using multichannel rather than single channel DVB-T signals. It may be proven in the near future that target classification of non-cooperative targets will be enabled by a high resolution DVB-T passive radar exploiting multichannel DVB-T signals and radar imaging.

REFERENCES

[1] Zoeller, C.L., Budge, Jr., M.C., and Moody, M.: “Passive coherent location radar demonstration”, Proc. Thirty-Fourth South-eastern Symp. on System Theory, 18–19 March 2002, pp. 358–362.

[2] H. D. Griffiths and C. J. Baker, “Passive Coherent Location radar systems. Part 1: Performance prediction.” Radar, Sonar and Navigation, IEE Proceedings, vol. 152, no. 3, pp. 124 – 132, 2005.

[3] C. J. Baker, H. D. Griffiths, and I. Papoutsis, “Passive coherent location radar systems. part 2: waveform properties,” Radar, Sonar and Navigation, IEE Proceedings -, vol. 152, no. 3, pp. 160–168, 2005.

[4] Di Lallo, A.; Farina, A.; Fulcoli, R.; Genovesi, P.; Lalli, R.; Mancinelli, R.; , "Design, development and test on real data of an FM based prototypical passive radar," Radar Conference, 2008. RADAR '08. IEEE , vol., no., pp.1-6, 26-30 May 2008

[5] M. Malanowsky, G. Mazurek, K. Kulpa, and J. Misiurewicz, "FM based PCL radar demonstrator", in Proc. IEEE International Radar Symposium, 2007. IRS 2007, Cologne Germany, 2007

[6] Malanowski, M.; Kulpa, K.; Misiurewicz, J.; "PaRaDe - PAssive RAdar DEmonstrator family development at Warsaw University of Technology," Microwaves, Radar and Remote Sensing Symposium, 2008. MRRS 2008 , vol., no., pp.75-78, 22-24 Sept. 2008

[7] Glende, M., Heckenbach, J., Kuschel, H., Müller, S., Schell, J., Schumacher, C.: “Experimental passive radar systems using digital illuminators (DAB/DVB-T”, Proc. of the International Radar Symposium (IRS 2007), Cologne, Germany, 05-07 September 2007.

[8] A. Capria, M. Conti, D. Petri, M. Martorella, F. Berizzi, E. Dalle Mese, R. Soleti, V. Carulli, “Ship Detection with DVB-T Software Defined Passive Radar”, Proceedings of 2010 IEEE GOLD Remote Sensing Conference, April 29-30, 2010, Italian Naval Academy, Livorno, Italy;

[9] Hongbo Sun; Tan, D.K.P.; Yilong Lu; , "Aircraft target measurements using A GSM-based passive radar," Radar Conference, 2008. RADAR '08. IEEE , vol., no., pp.1-6, 26-30 May 2008

[10] D. Petri, F. Berizzi, M. Martorella, E. Dalle Mese, A. Capria, “A Software Defined UMTS Passive Radar Demonstrator”, Proceedings of the International Radar Symposium (IRS) 2010, June 16-18, 2010, Vilnius, Lithuania;

[11] Guo, H.; Woodbridge, K.; Baker, C.J.; , "Evaluation of WiFi beacon transmissions for wireless based passive radar," Radar Conference, 2008. RADAR '08. IEEE , vol., no., pp.1-6, 26-30 May 2008

[12] Kuschel, H.; Heckenbach, J.; Muller, S.; Appel, R.; , "On the potentials of passive, multistatic, low frequency radars to counter stealth and detect low flying targets," Radar Conference, 2008. RADAR '08. IEEE , vol., no., pp.1-6, 26-30 May 2008

[13] Gould, Dale; Pollard, Robert; Sarno, Carlos; Tittensor, Paul; , "Developments to a multiband passive radar demonstrator system," Radar Systems, 2007 IET International Conference on , vol., no., pp.1-5, 15-18 Oct. 2007
[14] Schroeder, A.; Edrich, M.; Winkler, V.; , "Multi-illuminator Passive Radar performance evaluation," Radar Symposium (IRS), 2012 13th International , vol., no., pp.61-64, 23-25 May 2012
[15] Jackson, M.C.; , "The geometry of bistatic radar systems," Communications, Radar and Signal Processing, IEE Proceedings F , vol.133, no.7, pp.604-612, December 1986
[16] Tsao, T.; Weiner, D.; Varshney, P.; Schwarzlander, H.; Slamani, M.; Borek, S.; , "Ambiguity function for a bistatic radar," Time-Frequency and Time-Scale Analysis, 1992., Proceedings of the IEEE-SP International Symposium , vol., no., pp.497-500, 4-6 Oct 1992
[17] N. J. Willis, "Bistatic Radar", Scitech Publishing Inc, 2005
[18] Harms, H.A.; Davis, L.M.; Palmer, J.; , "Understanding the signal structure in DVB-T signals for passive radar detection," Radar Conference, 2010 IEEE , vol., no., pp.532-537, 10-14 May 2010
[19] Dario Petri, Amerigo Capria, Michele Conti, Fabrizio Berizzi, Marco Martorella and Enzo Dalle Mese (2012). High-range resolution multichannel DVB-T passive radar: aerial target detection. International Journal of Microwave and Wireless Technologies, 4, pp 147-153
[20] Poullin, D.; , "Passive detection using digital broadcasters (DAB, DVB) with COFDM modulation," Radar, Sonar and Navigation, IEE Proceedings - , vol.152, no.3, pp. 143- 152, 3 June 2005
[21] Cardinali, R.; Colone, F.; Ferretti, C.; Lombardo, P.; , "Comparison of Clutter and Multipath Cancellation Techniques for Passive Radar," Radar Conference, 2007 IEEE , vol., no., pp.469-474, 17-20 April 2007
[22] M. Di Dio; "Signal synchronization and channel estimation/equalization functions for DVB-T software-defined receivers" Tesi di Laurea Specialistica Ingegneria delle Telecomunicazioni Anno Accademico 2008/09 Università di Pisa
[23] Colone, F.; O'Hagan, D.W.; Lombardo, P.; Baker, C.J.; , "A Multistage Processing Algorithm for Disturbance Removal and Target Detection in Passive Bistatic Radar," Aerospace and Electronic Systems, IEEE Transactions on , vol.45, no.2, pp.698-722, April 2009
[24] Petri, D.; Moscardini, C.; Martorella M.; Conti M.; Capria A.; Berizzi F.; , "Performance Analysis of thr Batches Algorithm for Range-Doppler Map Formation in Passive Bistatic Radar," Radar 2012 International Conference on Radar System, 22-25 October 2012
[25] S.Haykin, "Adaptive Filter Theory", Prentice Hall, Upper Saddle River, New Jersey, fourth edition, 2002
[26] Palmer, J.E.; Searle, S.J.; , "Evaluation of adaptive filter algorithms for clutter cancellation in Passive Bistatic Radar," Radar Conference (RADAR), 2012 IEEE , vol., no., pp.0493-0498, 7-11 May 2012
[27] P. E. Howland, H. D. Griffiths and C. J. Baker, "Passive Bistatic Radar Systems", Chapter 7 in the book "Bistatic Radar: Emerging Technology", M. Cherniakov, John Wiley & Sons (2008).

[28] http://www.sdrforum.org/pages/documentLibrary/documents/SDRF-06-R-0011-V1_0_0.pdf

[29] http://www.ettus.com/home

[30] C. Baker, "Multistatic Radar Processing", NATO UNCLASSIFIED RTO-EN-SET-133, April, 2009